Fall 2018

An investigation into the effects of ion tracks on α-quartz

Bryant Alan Kanies

AN INVESTIGATION INTO THE EFFECTS OF ION TRACKS ON α-QUARTZ

by

BRYANT ALAN KANIES

A THESIS

Presented to the Faculty of the Graduate School of the

MISSOURI UNIVERSITY OF SCIENCE AND TECHNOLOGY

In Partial Fulfillment of the Requirements for the Degree

MASTER OF SCIENCE IN NUCLEAR ENGINEERING

2018

Approved by

Joseph Graham, Advisor
Ayodeji B. Alajo
Gary E. Mueller

ABSTRACT

The passage of a swift heavy ion through a material can cause columnar, amorphous nano-structures known as ion tracks. Swift heavy ions are present in a number of applications ranging from nuclear reactors to nuclear waste storage and onboard spacecraft. The study of ion tracks has been ongoing since the late 1950s and has led to several technological advancements. In fact, ion beams have been used to enhance material properties and aid in the production of electrical components. Ion beams, and their resultant ion tracks, can therefore be seen as a method to purposefully alter material properties such as thermal diffusivity. One method through which ion tracks can alter material properties is through the alteration of phonon transport. It is expected that phonons are spatially confined between ion tracks.

In this study, Z- and Y-cut α-quartz single crystalline samples were irradiated with 20 MeV nickel 6+ ions. These crystals were irradiated to nominal fluence values of 1.0×10^{9}, 1.0×10^{10}, and 1.0×10^{12} ions cm^{-2}. The crystals were irradiated with varying fluence values in order to understand how the spacing of ion tracks affects phonon transport. An Inelastic Thermal Spike model was also developed to model the track radii. The Thermal Spike model allows for the effects of track size to also be taken in to account. In addition, Raman spectroscopy was performed for each fluence value. The effects of ion tracks on phonon confinement were understood by examining how the peak parameters changed with increasing fluence and comparing the parameters to the phonon dispersion relations for α-quartz.

ACKNOWLEDGEMENTS

First and foremost, I would like to thank my lord and savior Jesus Christ for sustaining me in His abundant grace and mercy. Without Him none of this would be possible. I want to also offer my most sincere gratitude to my adviser, Dr. Graham. He guided me through this whole process and was an incredibly invaluable resource. I learned many difficult concepts and skills under his guidance. I also want to thank my other committee members, Dr. Alajo and Dr. Mueller. Throughout the years they have taught me many important concepts and aided me in other aspects of my life. I am also very grateful for all the help Maria Camila Garcia Toro provided with the AFM measurements.

I want to also take this opportunity to thank Olivia for her love and support. She keeps me on my toes and encourages me to step beyond my comfort zone. Additionally, none of this would be possible without the love and support of my family. To them I am extremely grateful for all that they do for me.

This work was made possible by NRC grant NRC-HQ-13-G-38-0026.

TABLE OF CONTENTS

Page

LIST OF ILLUSTRATIONS

Page

LIST OF TABLES

Page

1. INTRODUCTION

Damage caused by the interaction of radiation with matter, or radiation damage, is of great concern in many nuclear engineering applications. Radiation is present in virtually all facets of the field, and thus, it and its effects are critically important to understand. Radiation must be understood and protected against for the health and safety of workers and the public. With regards to safety and performance, it is also important for the effects of radiation on materials to be well understood.

Radiation can physically alter a material by causing various defects – new phases may be produced, voids formed, and swelling of the material may occur [[1], [2]]. These defects, in turn, can alter material properties such as ductility, strength, toughness, thermal conductivity, and chemical reactivity [1]. It is important to understand how radiation will affect a material to assure reliability of mission critical components exposed to radiation.

Radiation damage can be caused by all forms of ionizing radiation: alpha particles (α), beta particles (β), gamma rays (γ-ray), neutrons, protons, and higher energy 'heavy' ions [1]. Some or all of these forms of radiation are observed in a wide variety of applications. Nuclear fission reactors are the application most often associated with radiation. In a nuclear reactor, shielding, control, and structural components will all be subject to varying energies and fluences of neutrons and γ-rays [2]. In addition to the neutrons and γ-rays, the fuel and cladding in a nuclear reactor will also experience irradiation due to α particles and ions released in the fission process. Failure of a power producing nuclear reactor has potential to cause serious environmental impact – making it essential to ensure that all of its critical components will perform as expected when exposed

to radiation. In addition to safety, understanding the effects of radiation on various components helps predict reactor performance, minimize maintenance, and ultimately help maximize reactor lifetime [2]. Similarly, key fusion reactor systems will be subject to intense radiation. Extreme temperatures accompany this intense radiation presenting major barriers to the commercial viability of current fusion designs. Components in a fusion reactor will be subject to γ-rays, and plasma particles – such as neutrons, alpha particles, and other light ions [[2]–[4]]. Additionally, due to sputtering, heavier ions will also be present which can lead to further damage of the first wall and other components [[2], [3]]. These considerations highlight how an understanding of the effects of radiation is crucial in fusion reactor research.

Another application directly related to nuclear reactors is the storage of spent nuclear fuel and related waste. Long-lived waste can remain radioactive for thousands of years after use [[5], [6]]. There are several methods for storing or disposing of radioactive waste including geological repositories, on-site dry cask storage, rock melting etc. [[7]–[10]]. Safe storage of long lived wastes highlights the necessity to understand radiation damage. The materials used to store these wastes will be irradiated throughout their lifetime – in many cases, for thousands of years. This will inevitably result in radiation damage and therefore alteration of material properties. A waste form may be required to be chemically inert and corrosion resistant; over time, radiation damage may alter these properties [[5], [11]]. Failure of such storage could lead to environmental contamination. This again highlights how essential it is to understand the effects of radiation on material properties.

Nuclear reactors and radioactive waste are not the only application in which the understanding of radiation and its effects are crucial. Another application which has recently regained more prominence is that of space exploration or space technologies. While on Earth, radiation from space is of little concern; the Earth's magnetic field and atmosphere shield the majority of cosmic radiation [[12]–[14]]. However, beyond Earth's protection, astronauts, space stations, shuttles, satellites, probes, and rovers can be subject to solar flares, cosmic rays, and particles trapped in the Van Allen belt [[13], [14]]. Additionally, vehicles utilizing nuclear power, such as satellites and rovers using radioisotope thermoelectric generators (RTGs), and future space craft, must also shield themselves from the radiation they produce [[12]]. If not accounted for properly, the radiation present in space can damage computers and other sensitive electronics. While majority of the structural and mechanical components in spacecraft suffer little effects from space radiation, without proper functioning electronics, the entire mission may have to be aborted.

There are less industrial applications for which radiation and its effects must be well understood. For instance, there are applications of radiation in the medical field. Amongst other things, these applications include X-rays, external beam radiation therapy, and fast neutron therapy [[15]–[17]]. In all of these, the surrounding facilities and equipment will be exposed to radiation. Sensitive electronics and other components which are exposed to radiation are required for successful operation of the equipment. Components exposed to γ-rays and fast MeV neutrons will require an in-depth understanding of the effects of this radiation to ensure safe operation.

One final application which itself has unique uses is that of ion beam facilities. These facilities can be used for electronic component production, biological imaging, medicine, material analysis, ion implantation, and ion irradiation of target materials [[18]–[23]]. These facilities can produce ions with high energies, up to the GeV range in some cases. These ions can consist of anything from protons to uranium.

It is apparent that the effect of radiation can be detrimental and present in a variety of applications. In each of these applications, however, radiation is being used as an invaluable tool. For instance, nuclear reactors provide approximately 20% of the electricity in the U.S. [[2], [24]]. The use of radiation in the medical field provides CT scans, X-rays, and cancer therapy. Radiation can also be used for geological dating, structural imaging, and sterilization of foods [[25]–[27]].

With consideration to the necessity of understanding and the potential for further benefit, there is a particular type of radiation effect that presents itself as particularly interesting known as an ion track. Ion tracks are amorphous columnar nano structures imbedded within a solid matrix (as seen in Figure 1.1.). Ion tracks are caused by the passage of a swift heavy ion (SHI) through a material [[28], [29]]. Since SHIs can be present in nearly all of the applications previously mentioned, ion tracks may also be present. This highlights how important the understanding of the effects of ion tracks is. In fact, the study of ion tracks has been ongoing since the late 1950s. It has led to several technological developments including neutron dosimeters, solid state track detectors, chemical microanalysis of certain elements, filters separating biological cells, uranium geological dating, and means to examine the history and space environment of extraterrestrial objects

[[25], [29]]. In addition to these technological developments, and in a wider scope, the usage of ions to cause nano-structural alterations to materials has also been shown to enhance electronic properties, improve surface smoothness, hardness, and wear resistance of materials [[18]–[21]]. Ion beam modification of materials can therefore be used as a tool for tailoring material properties.

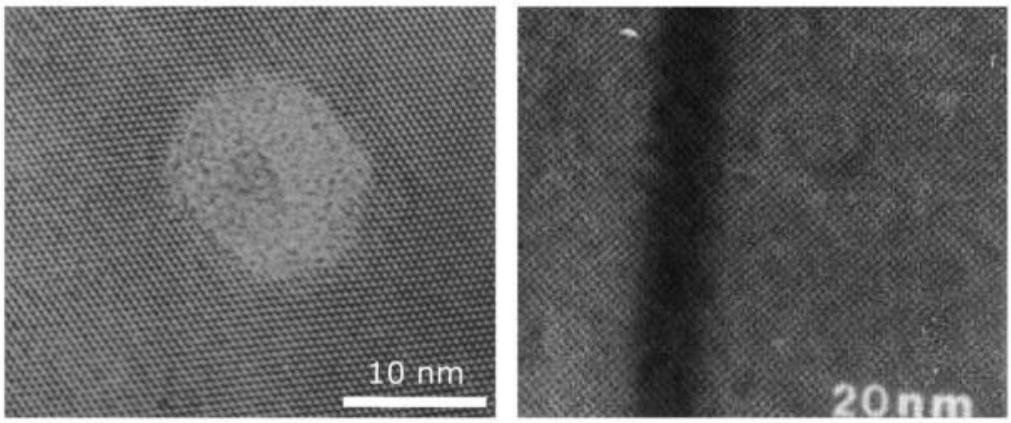

Figure 1.1. Example ion tracks. (Left) Cross section of a single ion track created by a Pb ion in mica. (Right) Continuous amorphous track created by trajectory of a Xe ion in $Y_3Fe_5O_{12}$. The darker gray is the amorphous track [[30]].

It is then desirable to understand how the passage of a SHI and its resultant track affect material properties. In hopes of tailoring materials' thermal properties, it is of particular interest to understand how these ions and tracks affect properties such as thermal diffusivity or thermal conductivity. The working hypothesis is that these nano structures affect the transport of phonons, quasi-particles of atomic lattice vibration that carry sound and heat, as they travel through a material. More specifically, it is believed that phonons

can be scattered or confined by various defects and nanostructures – including ion tracks [[31]–[35]]. The alteration of this phonon transport is significant because phonons are the method for which energy, or heat, is transferred throughout a solid [[31]].

The size, spacing, and amount of ion tracks are all suspected to have a role in the alteration of phonon transport. To begin investigating the contribution of each of these aspects, α-quartz (SiO_2) was irradiated in the Ion Beam Materials Laboratory (IBML) at the University of Tennessee Knoxville (UTK) [[36]]. Two different cuts of crystal were chosen for this project: Z- and Y- cut. α-quartz has a hexagonal crystal symmetry. This symmetry is defined by use of various axes and planes – including the x, y, and z axis as seen in Figure 1.2. A single crystal may be cut along or perpendicular to its planes and axes. To obtain a Z-cut crystal, the crystal is cut perpendicularly to its z-axis. Similarly, a Y-cut crystal is obtained by cutting perpendicularly to its y-axis. These different cuts were selected in order to better analyze in which direction phonon transport was modified the greatest. These samples were irradiated with Ni^{6+} ions at 20 MeV energy and nominal fluences of 1×10^{9}, 1×10^{10}, and 1×10^{12} ions cm^{-2}. The numerical modeling work of this project also supports future efforts to irradiate calcium fluoride (CaF_2). In order for ion track formation to occur in a material, the SHI must have an electronic stopping power (S_e) greater than a certain threshold [[28]]. These two materials were chosen due to their relatively low S_e threshold around 5 keV nm^{-1} [[28], [37], [38]].

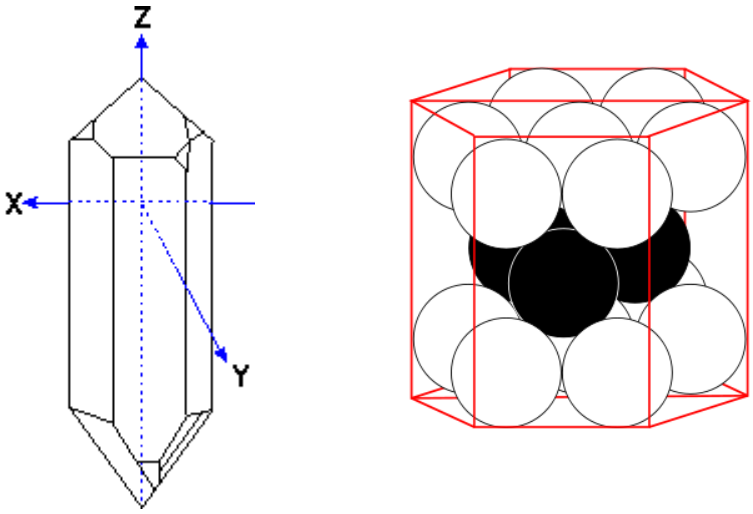

Figure 1.2. Quartz crystalline structure. (Left) An example of the quartz crystalline structure. The x, y, and z axes are indicated in this illustration [[39]]. Quartz is composed of multiple SiO_2 tetrahedron. (Right) An illustration of the hexagonal close packed structure of SiO_2 tetrahedron [[40]].

To analyze how the spacing and number of ion tracks affected phonon transport, Confocal Raman and Atomic Force microscopy (CRM and AFM respectively) were performed. In addition to these techniques, an Inelastic Thermal Spike (i-TS) and SRIM/TRIM models were created. These models are intended to allow for a better understanding of the size of the ion tracks. These techniques and models allow for the construction of a framework on which a deeper understanding of how altered phonon transport affects thermal properties of materials will be gained.

1.1. ION TRACK FORMATION

The passage of a swift heavy ion through a material can lead to defects, columnar amorphous tracks (ion tracks), and other nano-structures [[28]]. Although the definition varies from research community to research community, a broadly inclusive definition of

a SHI is any ion heavier than an α particle of high. These typically consist of transition metals or heavier elements. It has been shown that SHIs must have an electronic stopping power (S_e) above a certain threshold to cause permanent structural modifications [[28]].

As a SHI passes through a material, it causes the ionization and ejection of delta-rays (δ-rays) due to its S_e [[28]]. These δ-rays are energetic, excited electrons which move rapidly away from the ion's trajectory or track center causing a cascade of ionization. The SHI also causes primary knock on atoms (PKAs) due to its nuclear stopping power (S_n). These ionizations and PKAs lead to high levels of disorder and local energy deposition in a material's lattice. The lattice then goes through 6 stages of recovery: 1. Charge Redistribution, 2. Charge Neutralization, 3. Electronic Relaxation, 4. Lattice Relaxation, 5. Heating Stage, and 6. Cooling Stage [[28]]. This is artistically depicted in Figure 1.3.

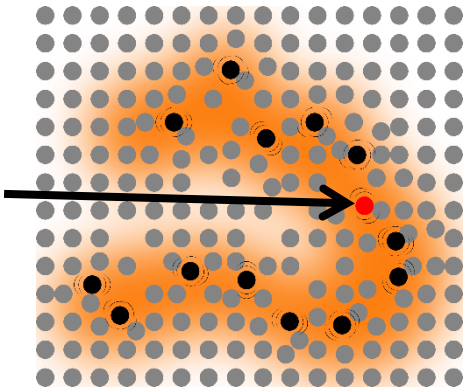

Figure 1.3. The passage of an ion. This is an artistic illustration of the passage of an ion through a lattice of atoms.

It is believed that track formation begins during the Lattice Relaxation stage [[28]]. Several models have been proposed to explain the track formation to varying degrees of success. Some of these include the Thermal Spike, Coulomb Explosion, Bond Weakening, and Exciton Self-Trapping models [[28]]. The i-TS model has often been favored because of its predictive power and will be discussed in greater detail later. It assumes that defects and tracks are formed during the heating stages as a molten phase forms along the ion trajectory. This molten phase is then rapidly quenched, leading to the amorphous columnar nano-structure. The Coulomb Explosion model relies on the explanation that as electrons are excited and ejected from the track trajectory, a large positive charge results in the center. This charge is due to the accumulation of positive ions which are rapidly dispersed due to the Coulomb force. Bond Weakening explains track formation and lattice damage through instability due to weakened bonds. The bonds between atoms are weakened because the electrons used for bonding have been excited and ejected away. In fact, it has been shown that a 15% excitation of valence electrons leads to lattice instability [[28]]. Exciton self-trapping describes electron-hole pairs being trapped on a dislocation or other defect. This trapping results in a local energy deposition and resultant deformation.

As mentioned previously, an ion track is an amorphous, columnar nano structure. These tracks consist of a cylinder with a diameter of a few nanometers comprised of an amorphous center surrounded by a defect halo [[37], [41], [42]]. The defect halo is a region consisting of partially amorphized crystal and other defects. The tracks will be continuous if the SHI has sufficient S_e; otherwise, the track may consist of several regions of amorphous crystal [[43]]. Additionally, the creation of an ion track may create a nano-hillock on the surface of the material. This hillock consists of lower density amorphous

material pushed out of the molten track core; its height can reach up to several nanometers [[44]]. These are illustrated in Figure 1.4.

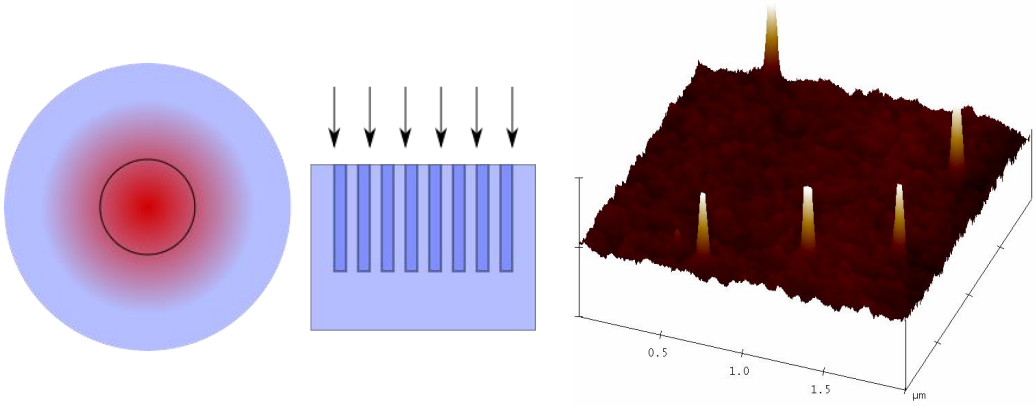

Figure 1.4. Illustration of ion tracks and nano-hillocks. (Right) An illustration highlighting the cylindrical nature of ion tracks. The circle in the center represents the area which was heated high enough to cause melting in the crystalline material. (Center) The arrows depict an incident fluence of ions. These ions result in columnar tracks, as seen by the darker cylindrical regions, which extend into the material. (Right) 3D view plot of nano-hillocks which result as a low density, molten phase is ejected from the crystal and then rapidly quenched.

1.2. QUALITATIVE PHONON TRANSPORT

Phonons are quantized elastic waves or lattice vibrations and are carried through an atomic lattice [[45]]. Phonons in a defect-free crystal can be described by the following wave function:

$$\Phi(\mathbf{r})=\mathbf{u}(\mathbf{q_0})\exp(-i\mathbf{q_0}\cdot\mathbf{r}) \quad (1)$$

where **u** is the polarization of the vibration and $\mathbf{q_0}$ is the wave vector. There are two main modes of vibration in materials; these modes are represented by two types of phonons: acoustic and optical. Various allowed normal modes of vibration arise for different crystalline structures [[46]]. The allowed vibrations are dictated by bond angle, the shape and type of bonding, and the mass, charge, and spacing of the constituent atoms. The total number of allowed normal modes (degrees of freedom) can be determined by:

$$3N-6 \quad (2)$$

where N is the total number of atoms in a molecule. This equation arises as a result of each atom possessing the ability to move in the x, y, and z directions. Phonons may involve molecular rotation, stretching or compression of bonds, translational motion of atoms, and other combinations of such motion.

The dispersion relation is a convenient tool for examining phonons in a material. The dispersion relation describes the relationship between the wave vector and frequency of a phonon. This relation can be plotted in various ways and along several crystallographic directions as in Figure 1.5. This proves to be a useful tool when examining the alteration of phonon transport through materials.

The aforementioned wave function is only applicable in ideal crystals with perfect harmonic interatomic potentials and long range order – meaning that the crystals are free of defects and boundaries. In more realistic situations, phonons can become partially localized (confined) or scattered between interfaces, grain boundaries, and other defects [[35]]. Since phonons are the method for energy transport through a material, the process

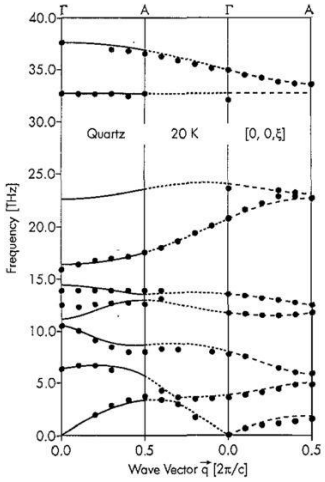

Figure 1.5. Phonon dispersion curves for α-quartz. This plot was obtained from the work of Strauch et al. [[47]].

of scattering or localization will likely lead to alterations in the thermal properties of a material. To illustrate the potential ways in which altered phonon transport may affect material properties, it is instructive to examine the model proposed by Joseph Callaway in 1959 [[31]]. This model was proposed to determine the thermal conductivity of a lattice. The model is represented by Equation 3.

$$\kappa = \frac{K}{2\pi^2 v_a}\left(\frac{KT}{\hbar}\right)^3 \left\{ \int_0^{\frac{\theta}{T}} \frac{\tau_c x^4 e^x}{(e^x-1)^2}\,dx + \frac{\left[\int_0^{\frac{\theta}{T}} \frac{\tau_c}{\tau_n}\frac{x^4 e^x}{(e^x-1)^2}\,dx\right]^2}{\int_0^{\frac{\theta}{T}} \frac{1}{\tau_n}\left(1-\frac{\tau_c}{\tau_n}\right)\frac{x^4 e^x}{(e^x-1)^2}\,dx} \right\} \tag{3}$$

In this equation, K is Boltzmann's constant, v_a is the velocity of sound, θ is the Debye temperature, $\hbar$ is the reduced Planck constant, T is the temperature in Kelvin, and $x = \hbar\omega/KT$ is a dimensionless phonon energy with ω being the phonon frequency. It is

important to note the term τ_c. This term represents the combined phonon relaxation time and is given by Equation 4.

$$\tau_c^{-1}=\tau_u^{-1}+\tau_N^{-1}+\tau_D^{-1}+\tau_B^{-1} \quad (4)$$

The four terms τ_u^{-1}, τ_N^{-1}, τ_D^{-1}, and τ_B^{-1} represent the relaxation times associated with Umklapp, normal 3-phonon, defect, and boundary scattering of phonons. Defect and boundary scattering occur when phonon transport is altered by the presence of a crystalline defect or boundary. Normal scattering is the process of phonons interacting with one another, and Umklapp scattering occurs when phonons interact and produce a phonon outside of the first Brillouin zone. Through consideration of this example, it is clear that the alteration or presence of new boundaries and defects in a lattice will alter the thermal conductivity of a material. This alteration or creation of new defects and boundaries will occur with the creation of ion tracks. To be able to successfully tailor material properties with ion beams, it must be understood how ion tracks affect phonon transport.

1.3. RAMAN SPECTROSCOPY

Raman spectroscopy is a powerful tool for investigating the vibrational properties of a material. A Raman spectrum is created by scattering an incident laser on a sample. As the laser photons inelastically scatter off the sample, approximately 1×10^{-5} of the original beam intensity is Raman scattered [[46]]. Raman scattering was discovered by Sir Chandraskera Venkata Raman in 1928 and is the process of light momentarily interacting with a molecule, causing transitions between vibrational levels in the molecule [[46]]. Raman scattering is contrasted with Rayleigh scattering; Raman scattering is inelastic while Rayleigh scattering is elastic.

Raman scattering is classically explained as follows [[46]]. The incident laser creates an electromagnetic field which fluctuates with time:

$$E=E_0 \cos(2\pi\nu_0 t) \tag{5}$$

where ν_0 is the frequency of the field, t is the time, and E_0 is the vibrational amplitude of the field. As the laser interacts with the molecule, an electric dipole moment is induced:

$$P=\alpha E \tag{6}$$

In this equation, P represents the dipole moment and α is the polarizability. The polarizability of a molecule is essentially the description of how distorted a molecule's electron cloud becomes in the presence of an electric field. Distortion is caused when the low mass charged electrons are slightly displaced by the electric field of the incident photons. Similarly, the negative charges may be attracted to external positive charges or repelled from other negative charges. The polarizability is represented by a tensor resulting in a spatially dependent dipole moment:

$$\begin{bmatrix} P_x \\ P_y \\ P_z \end{bmatrix} = \begin{bmatrix} \alpha_{xx} & \alpha_{xy} & \alpha_{xz} \\ \alpha_{yx} & \alpha_{yy} & \alpha_{yz} \\ \alpha_{zx} & \alpha_{zy} & \alpha_{zz} \end{bmatrix} \begin{bmatrix} E_x \\ E_y \\ E_z \end{bmatrix} \tag{7}$$

The underlying symmetry of the crystal, this polarizability tensor, and its derivatives with respect to atomic displacement determine whether or not a particular phonon mode is Raman active. If the molecule is vibrating with a frequency of ν_m, its nuclear displacement can be represented in this way:

$$q=q_0 \cos(2\pi\nu_m t) \tag{8}$$

Here, q_0 is the vibrational amplitude. If the vibrational amplitude is small, α can be written as a linear function of q, with α_0 representing the polarizability at the equilibrium position. Then, it can be shown that the dipole moment of the molecule can be written as:

$$P=\alpha_0 E_0 \cos(2\pi\nu_0 t)+\frac{1}{2}\left(\frac{\partial\alpha}{\partial q}\right)_{q=0} q_0 E_0[\cos\{2\pi(\nu_0+\nu_m)t\}+\cos\{2\pi(\nu_0-\nu_m)t\}] \quad (9)$$

This equation is a representation of oscillating dipoles radiating light. The first term in the equation represents the contribution from Rayleigh scattering, light emitted at the same frequency as the incident laser ν_0. The second term is representative of an oscillating dipole emitting light with frequency $\nu_0 \pm \nu_m$ and represents the contribution from Raman scattering.

Additionally, Raman scattering can be explained through the usage of energy levels and molecular excitation. This description also coincides with the fact that phonons are the quantum of vibrations. The transition from one molecular energy level to another can be described by the following relationship:

$$\Delta E=h\nu \quad (10)$$

In this relationship, ΔE is the change in energy from one level to another, h is Planck's constant and ν is the vibrational frequency. As a photon from the laser (frequency ν_0) interacts with the molecule, the molecule may gain or lose energy corresponding to an allowed energy level. This energy level corresponds to a frequency of ν_m. It is important to note that each of these allowed energy levels corresponds to a Raman-active vibrational mode, or phonon. Thus, in Raman scattering, the incident photon may transfer enough energy to the molecule to excite it into a higher molecular energy

level and then be reemitted. The Raman scattered light would then leave the system with a frequency of $\nu_0 - \nu_m$. Conversely, the molecule may impart energy to the incident photons. This would result in a change in frequency of $\nu_0 + \nu_m$. A diagram depicting this process can be seen in Figure 1.6. When these frequencies are converted to their corresponding wave numbers and subtracted from the wave number of the incident laser, they are called Raman shifts. Raman shifts resulting from $\nu_0 - \nu_m$ are called Stokes lines while Raman shifts from $\nu_0 + \nu_m$ are called anti-Stokes lines.

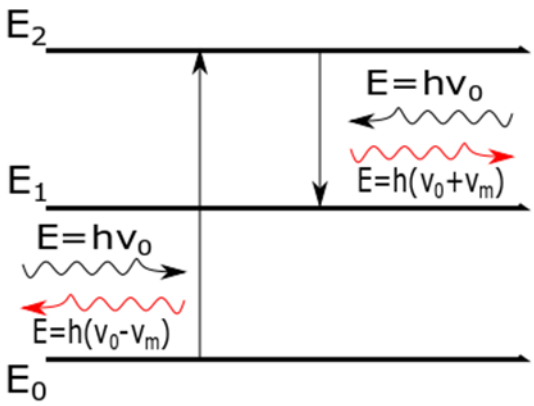

Figure 1.6. An example molecular energy level diagram. This diagram represents the transition of vibrational energy levels due to incident laser photons. The transition from E_0 to E_2 will result in a Stokes line on the Raman spectra. The transition from E_2 to E_1 will result in an anti-Stokes line.

The following steps provide a general outline for obtaining a Raman spectrum:

1. Coherent light photons (i.e. a laser) is shone onto a sample
2. The light is scattered and collected by an objective lens

3. The Rayleigh contribution to the scattered light is filtered using either a notch or edge filter
4. A spectrograph then analyzes the light via a diffraction grating and detector in order to separate it into different wavelengths

Light entering the detector with the same frequency as the incident light is Rayleigh scattered light. Light entering the detector which has a different frequency than the incident laser has been Raman scattered. The intensity of the light which has been Raman scattered is then plotted against its Raman shift (see Figure 1.7). Photons which impart energy to molecules result in Stokes lines or positive Raman shifts. Negative Raman shifts result in Anti-Stokes lines [[46]]. Raman spectroscopy can be performed using a microscope or in bulk. The use of a confocal microscope allows for diffraction limited resolution in the beam direction.

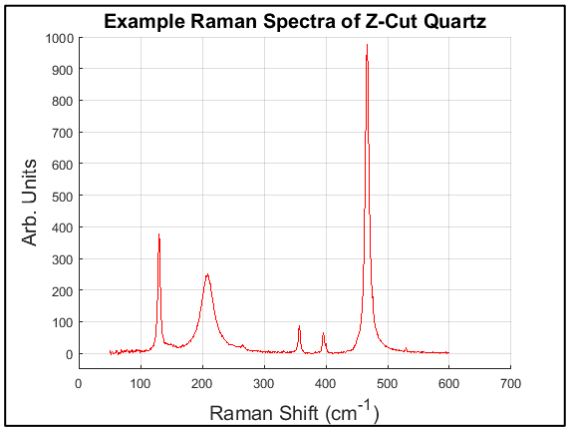

Figure 1.7. Raman spectrum of a Z-cut α-quartz crystal.

Raman microscopy is a powerful technique for probing vibrational properties, phase, crystal structure, local bonding, and defects on the micron and submicron scales [[21], [48]]. This is because the peaks appearing on Raman spectra directly correspond to Raman-active phonons. Thus, as materials are altered, changes in their Raman spectra indicate changes to its molecular structure. In fact, Raman spectroscopy can be used in-situ for determining how a process is altering a material [[21], [46]].

In the present study, Raman spectroscopy is used to analyze how phonon transport is being altered with the introduction of ion tracks. As mentioned previously, phonon dispersion curves are a representation of the relationship between phonon frequency and wave vector – in other words, the energy-momentum relations for phonons. By examination of a Raman spectrum, the frequency of a Raman-active phonon can be directly determined. Once the Raman-active phonons are determined from the Raman spectra, they can be matched to their respective dispersion curves, hence phase, composition and orientation. Analysis of the Raman spectrum and dispersion curves can be indicative of how the phonon's transport is being altered.

There are several effects which an ion track may have on phonon transport. One possibility is that phonons will be spatially confined between ion tracks. This spatial confinement can be seen through a broadening of the Raman peaks. The broadening of the peaks is due to a loss of long range crystalline order [[49]]. The presence of ion tracks and other defects could lead to a decrease in the phonon lifetime due to scattering or phonon confinement; this causes uncertainty in the phonon momentum and an increased range of wave numbers to contribute to the Raman spectra [[33], [34], [48]–[50]]. The effects of

phonon confinement can be qualitatively observed through phonon dispersion curves. By identifying the frequency associated with a phonon through its Raman peak, the associated phonon can be identified on the dispersion curve. The plot of the dispersion relation for the phonon can then be used to reveal how the ion tracks are affecting phonon transport. If the dispersion relation is a slanted straight line through the Brillouin zone or there is curvature to the line it is likely that the Raman peak will broaden. This is an indication that the phonon is likely being confined by the ion tracks. A broadening of the Raman peak indicates that a broader range of photon frequencies is contributing to the peak and thus more phonon wave vectors. Asymmetric broadening of the Raman peak is likely a result of the curvature of the dispersion relation. If the dispersion relation is represented by a horizontal line with almost zero slope, there will likely be no change in the Raman peak due to the presence of ion tracks. The expectation is that as the irradiation fluence increases the effects of phonon confinement will become more pronounced. This is due to the increased presence and proximity of the ion tracks created by the Ni ions.

Several studies have been performed which have consistent results with the aforementioned arguments. The broadening of Raman peaks has been associated with an increasing ion fluence in the work performed by Myers et al., Compagnini et al., Hunn et al., Orwa et al., Bajwa et al., Liu et al., Nagabhushana et al., and Costantini et al. [[22], [33], [34], [49], [51]–[54]]. Additionally, it has been demonstrated that Raman peaks may shift frequencies altogether – from one Raman shift to another either higher or lower on the spectrum [[33], [51], [53], [55], [56]]. This indicates that phonon transport may also be altered by stresses produced in a material. The effects which stress have on unirradiated α-quartz has been shown by Hemley [[55]]. In this study, external pressure produced a

compressive stress in the samples; this resulted in a blue shift of the Raman spectra. These shifts could be caused by an alteration of the phonon wavelength. For compressive stresses it could be concluded that compression causes a shortening of the wavelength and therefore an increase in the wave vector – a blue shift on the Raman spectra. This could indicate that as a material is compressed, long range order could be lost. Additionally, it could then be concluded that if the presence of ion tracks results in a shift of the Raman spectra, they are causing stresses in a material. Finally, it has also been demonstrated that previously allowed vibrational modes may be erased or new vibrational modes may arise in the presence of ion tracks [[22], [34], [49], [53], [54], [57]].

2. MODELING

In order to gain a better understanding of the formation of ion tracks and to help predict track size, an inelastic Thermal Spike model and a SRIM/TRIM model were created. The i-TS model was created using MATLAB and focused on determining the track radius in both α-quartz (SiO_2) and calcium fluoride (CaF_2) based on a range of electronic stopping powers. The SRIM/TRIM model was created using SRIM 2008 and focuses on calculating the stopping power and range of nickel ions in SiO_2 and CaF_2 [[58]].

2.1. INELASTIC THERMAL SPIKE MODEL

The i-TS model is a two-temperature approach which couples the electronic temperature to the lattice atom temperature developed quantitatively by Izui [[28], [42]]. It is often favored in predicting ion track radii due to its consistent success compared to other models [[41], [42], [44], [59], [60]]. The i-TS model also has the advantage of successfully describing the electronic stopping power threshold required for track formation [[59]]. The i-TS model assumes that defects and tracks are formed during the heating stages as a molten phase forms along the ion trajectory. This molten phase is then rapidly quenched, leading to the amorphous columnar nano-structure.

2.1.1. Methodology. The Thermal Spike Model is governed by two coupled heat equations given as follows:

$$C_e \frac{\partial F}{\partial t} = \nabla \cdot (K_e \nabla F) - g(F-G) + A(r,t) \tag{11}$$

$$C_a \frac{\partial G}{\partial t} = \nabla \cdot (K_a \nabla G) + g(F-G) \tag{12}$$

In these equations, F is the electronic temperature and G is the lattice temperature. C_e, K_e, C_a, and K_a represent the volumetric heat capacity and the thermal conductivity of the electronic system and lattice respectively. The electron-phonon coupling parameter is represented by g. The term A(r,t) represents the heat generation term from δ-ray production, which varies with time, t, radius, r, and is dependent on the incident ion's stopping power , S_e. A(r,t) is given by the following [[61]]:

$$A(r,t)=BD(r)\alpha \exp(-\alpha t) \tag{13}$$

$$\iint_{0,0}^{\infty,r_m} A(r,t)\, 2\pi r\, dr\, dt=S_e \tag{14}$$

where B is a normalization factor and D(r) is the radial dose distribution of δ-rays derived by Waligorski et al. [[62]]. α is given as $1/\tau$, τ is 10^{-15} s representing the electronic relaxation time, and r_m corresponds to the maximum range for δ-rays projected perpendicularly to the ion trajectory. In the proceeding equation, the Bethe formula was used to calculate S_e. It is given as:

$$S_e=-\frac{dE}{dx}=\frac{4\pi k_0^2 Z^2 e^4 N}{mc^2\beta^2}\left[\ln\left(\frac{2mc^2\beta^2}{I(1-\beta^2)}\right)-\beta^2\right] \tag{15}$$

Here N is the electronic number density, mc^2 is the rest mass of an electron, e is the elementary charge, β is the ratio of the incident ion's velocity to the speed of light (v/c), Z is the atomic number of the ion, and I is the mean excitation energy of the medium in eV. If k_0^2 is written instead as $\frac{1}{4}\pi\epsilon_0$, Equation 15 becomes:

$$S_e = \frac{4\pi z^2 N}{mc^2\beta^2}\left(\frac{e^2}{4\pi\epsilon_0}\right)^2 \left[\ln\left(\frac{2mc^2\beta^2}{I(1-\beta^2)}\right) - \beta^2\right] \quad (16)$$

where ϵ_0 is given as 8.54×10^{-12} F/m or $C^2/(J\ m)$. *I* requires an understanding of the system which the ion is passing through. The mean excitation energy (in unites of eV) is given by [[63]]:

$$I \cong \begin{cases} 19.0, & Z=1 \\ 11.2+11.7\ Z, & 2\leq Z\leq 13 \\ 52.8+8.71\ Z, & Z>13 \end{cases} \quad (17)$$

For a compound mixture with number density n_i, the mean excitation energy can be found by:

$$\left(\sum_i n_i Z_i\right) * \ln(I) = \sum_i n_i Z_i \ln(I_i) \quad (18)$$

This indicates that $\sum n_i Z_i$ is the number of electrons in the medium, and the equation for mean excitation energy can be written as:

$$N * \ln(I) = \sum_i n_i Z_i \ln(I_i) \quad (19)$$

It can be shown, then, that the ratio $n_i Z_i/N$ is the ratio of the electrons belonging to one constituent atom to the total number of electrons present. If p_i is the number of electrons present for element i, then this can be simplified then to this relationship:

$$\frac{N_i Z_i}{n} = \frac{p_i}{\sum_i p_i} \quad (20)$$

For example, a water molecule has 10 total electrons. Because there are two hydrogen atoms, there are two electrons present due to hydrogen, and 8 due to oxygen. Thus p = 2 for H, and 8 for O. The ratio of $n_i Z_i/N$ for hydrogen is then given as [[63]]:

$$\frac{p_i}{\sum_i p_i} = \frac{2}{2+8} = \frac{2}{10} \tag{21}$$

This simplifies the expression for *I* as follows:

$$I = \exp\left(\frac{\sum_i p_i \ln(I_i)}{\sum_i p_i}\right) \tag{22}$$

Given the ion energy, E, the ratio of velocities, β, can be determined by:

$$\beta = \sqrt{1-\left(\frac{m_0 c^2}{m_0 c^2+E}\right)^2} \tag{23}$$

Given an electronic number density in electrons cm^{-3}, a more convenient way to express the stopping power is as follows:

$$S_e = 5.09913\times10^{-29}\frac{Z^2 N}{\beta^2}\left[\ln\left(\frac{1.022\times10^6\beta^2}{I\left(1-\beta^2\right)}\right)-\beta^2\right] \text{[KeV/nm]} \tag{24}$$

The distribution of heat from an incident ion is preliminarily distributed radially by the ejection of δ-rays. This distribution is described by Waligorski et al. and is derived as follows [[62]]:

$$D(r) = D_1(r)\left(1+K(r)\right) \tag{25}$$

$$D_1(r)=\frac{Ne^4Z^{*2}}{\alpha mc^2\beta^2 r}\left[\frac{\left(1-\frac{t+\theta}{T+\theta}\right)^{\frac{1}{\alpha}}}{t+\theta}\right] \tag{26}$$

$$K(r)=A\left(\frac{r-B}{C}\right)\exp\left(-\frac{r-B}{C}\right) \tag{27}$$

$$K(r)=0, \text{ for } r<0.1 \text{ nm} \tag{28}$$

N, β, and mc^2 are the same as before. Here, Z* is the effective charge of the incident ion, r is the radial distance from the trajectory of the ion, t is the radial distance multiplied by the material's density, and B is equal to 0.1 nm. A and C are given by Equations 29 and 30

$$A=\begin{cases} 8\times\beta^{\frac{1}{3}} \text{ for } \beta<0.03 \\ 19\times\beta^{\frac{1}{3}} \text{ for } \beta\geq 0.03 \end{cases} \tag{29}$$

$$C=1.5 \text{ nm}+5 \text{ nm}\times\beta \tag{30}$$

In this relationship, the Rutherford cross-section for δ-ray production from atoms with ionization potential I = 10 eV is assumed. Additionally, normal ejection and a power law range energy relationship are used. α is a parameter ultimately dependent on β, θ (g cm^{-2}) is the range of a δ-ray with energy of 10 eV, and T (g cm^{-2}) is the maximum range of δ-rays in a material. The range of a δ-ray with an energy of 10 eV, θ, has been calculated to be 4.17×10^{-8} g cm^{-2}. To calculate T, the maximum δ-ray energy is first determined:

$$W=\frac{2mc^2\beta^2}{1-\beta^2} \tag{31}$$

Then, T can be calculated:

$$T=kW^{\alpha} \tag{32}$$

$$\alpha=\begin{cases}1.079, & \beta<0.03\\ 1.667, & \beta>0.03\end{cases} \tag{33}$$

$$k=6\times10^{-6}\,\frac{g}{cm^2}\,keV^{-\alpha} \tag{34}$$

Finally, the effective charge of the ion can be determined using the equation proposed by Pierce and Blann [[64]]. In this equation the velocity of the ion, v, can be deduced from β, and v_0 is Bohr's velocity or $\approx 2.2\times10^6$ m/s.

$$Z_{eff}=Z^{*}=Z\left(1-\exp\left(-\frac{v}{v_0}Z^{-\frac{2}{3}}\right)\right) \tag{35}$$

Returning to Equation 11, expanding it by substituting the cylindrical Del operator and realizing that for a homogenous crystal cylindrical symmetry can be assumed:

$$C_e\frac{\partial F}{\partial t}=\frac{1}{r}\left(\frac{\partial}{\partial r}\right)\left(rK_e\frac{\partial}{\partial r}F\right)-g(F-G)+A(r,t) \tag{36}$$

Using a forward time difference scheme and diamond difference scheme in radius, Equation 36 can be written as:

$$\begin{aligned}C_{e,i,n}\frac{F_{i,n+1}-F_{i,n}}{\Delta t}=&K_{e,i,n}\frac{F_{i+1,n}-F_{i,n}}{\Delta r^2*i}+\frac{(K_{e,i+1,n}-K_{e,i,n})(F_{i+1,n}-F_{i,n})}{\Delta r^2}\\&+K_{e,i,n}\frac{F_{i+1,n}-2F_{i,n}+F_{i-1,n}}{\Delta r^2*i}-g\left(F_{i,n}-G_{i,n}\right)+A_{i,n}\end{aligned} \tag{37}$$

In this equation, i represents the spatial steps while n represents the time steps. This equation can be simplified and applied to the lattice temperature to result in Equations 38 and 39.

$$F_{i,n+1}=F_{i,n}+\frac{\Delta t}{C_{e,i,n}}\left[\left\{\frac{1}{\Delta r^2}\left[\begin{matrix}(F_{i+1,n}-F_{i,n})\left(K_{e,i,n}\left(\frac{1}{i}\right)\right)\\ +K_{e,i,n}(F_{i+1,n}-2F_{i,n}+F_{i-1,n})\end{matrix}\right]\right\}-g(F_{i,n}-G_{i,n})+A_{i,n}\right] \quad (38)$$

$$G_{i,n+1}=G_{i,n}+\frac{\Delta t}{C_{a,i,n}}\left[\frac{1}{\Delta r^2}\left\{\begin{matrix}(G_{i+1,n}-G_{i,n})\left((K_{a,i+1,n}+K_{a,i,n}\left(\frac{1}{i}-1\right)\right)\\ +K_{a,i,n}(G_{i+1,n}-2G_{i,n}+G_{i-1,n})\end{matrix}\right\}+g(F_{i,n}-G_{i,n})\right] \quad (39)$$

The stability of this method is limited by Equation 40. The stability criterion must be satisfied for both the electron or lattice thermal conductivity and resistivity [[42]].

$$\frac{K\Delta t}{C\Delta r^2}<\frac{1}{2} \quad (40)$$

where

$$K_e=D_eC_e \quad (41)$$

$$C_e=\frac{3}{2}n_ek \quad (42)$$

Equation 41 describes the relationship for the electron thermal conductivity, and Equation 42 describes the volumetric heat capacity of the electrons [[65]]. By assuming a value for n_e of 5×10^{22} electrons cm^{-3}, C_e becomes 1 J $cm^{-3}K^{-1}$ [[65]]. Additionally, D_e is equal to 2 cm^2/s [[65]]. Following a convergence study and in order to maintain the stability criteria, a spatial step size, Δr, of 0.5 nm and a temporal step size, Δt, of 5.625×10^{-16} s were chosen.

The volumetric heat capacity and thermal conductivity for the SiO_2 lattice are given in Equations 43-46 [[59]]. These values are temperature dependent. The density, ρ, melting

temperature, T_m, electron-phonon mean free path, λ, and latent heat of fusion, L_{hf}, of SiO_2 and CaF_2 are given in Table 2.1.

$$K_a = \frac{14}{T^{0.9}} \quad \text{for } T>100K \tag{43}$$

$$K_a = 0.01 \quad \text{for } T>T_m \tag{44}$$

$$C_a = \left(3.3\cdot 10^{-4}T + 0.65\right)\rho \quad \text{for } T>100K \tag{45}$$

$$C_a = 0.42\rho \quad \text{for } T>T_m \tag{46}$$

Table 2.1. Various properties of SiO_2 and CaF_2.

Material	ρ	T_m	λ	L_{hf}
	g cm^{-3}	K	nm	J g^{-1}
SiO_2	2.62	1972	4.0	140
CaF_2	3.18	1691	3.7	220

To obtain the lattice thermal conductivity and volumetric heat capacity functions for CaF_2, a Lagrangian interpolation function was used. The inputs for this function were obtained from Plata et al. and Qi et al. [[66], [67]]. These are seen in Figure 2.1. and summarized in Table 2.2.

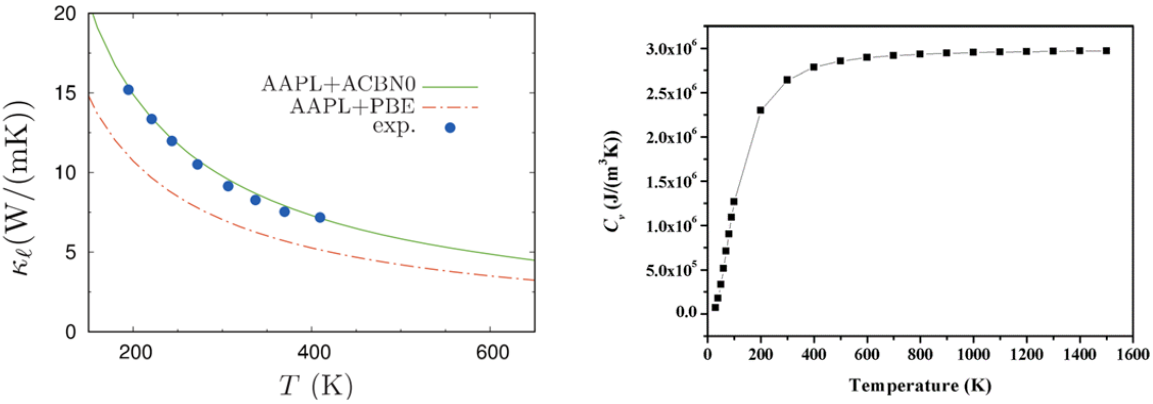

Figure 2.1. Plots use to calculate K_a and C_a for CaF_2. These plots were obtained from (left) Plata et al. and (right) Qi et al. [[66], [67]].

Table 2.2. Data points used in calculating Ca and Ka for CaF_2.

T	K_a	C_a
K	W cm^{-1} K^{-1}	J cm^{-3} K^{-1}
200	0.15	-
249	0.12	-
300	0.08	-
400	0.06	2.75
800	-	2.88
1000	-	2.9
1500	-	2.9

From these inputs, the following equations and the coefficients seen in Table 2.3 were derived:

$$K_a = \begin{cases} AT^3 - BT^2 + C\,T - D, & T < 400\ K \\ 0.05, & T \geq 400\ K \end{cases} \quad (47)$$

$$C_a = AT^3 - BT^2 + CT - D \quad (48)$$

Table 2.3. Constants computed for C_a and K_a of CaF_2. These were computed using a Lagrangian polynomial.

Parameter	K_a W cm^{-1} K^{-1}	C_a J cm^{-3} K^{-1}
A	2.80×10^{-8}	3.97×10^{-10}
B	2.27×10^{-5}	1.08×10^{-6}
C	5.32×10^{-3}	7.79×10^{-4}
D	2.31×10^{-1}	1.38×10^{-2}

To determine heat capacity and thermal conductivity for molten CaF_2, the conductivity and specific heat at the melting temperature of SiO_2 was determined using Equations 45 and 46. The values of K_a and C_a for molten SiO_2 from Equations 45 and 46 were then divided by the evaluated parameters to obtain the ratios of molten C_a to solid C_a and liquid K_a to solid K_a. These were determined to be 0.3229 and 0.6596 respectively. Then, evaluating Equations 47 and 48 at the melting temperature of CaF_2 and multiplying by these ratios, the liquid K_a and C_a of CaF_2 were obtained:

$$K_a = 0.033 \quad \text{for } T > T_m \quad (49)$$

$$C_a = 0.042 \quad \text{for } T > T_m \quad (50)$$

The last parameter required is the electron phonon coupling, g. This term governs the rate of electron energy relaxation towards the lattice [[60]]. It determines how well energy is transferred from the excited electrons to the lattice. It is given by [[44]]:

$$g=\frac{D_e C_e}{\lambda^2} \tag{51}$$

λ is the electron-phonon mean free path and has been determined experimentally [[44]]. The boundary conditions used to evaluate the i-TS model are as follows:

$$\frac{\partial T}{\partial r}_{r=0}=0 \tag{52}$$

$$\frac{\partial T}{\partial r}_{r=40}=0 \tag{53}$$

$$T(t=0)=300K \tag{54}$$

This scheme calculates the temperature of the lattice atoms for each 0.5 nm radial step up to 40 nm at each temporal step from 1 fs up to 1778 fs. In addition to that, these values are determined over a range of stopping powers. The assumption while using the i-TS model is that as an ion imparts its energy to a lattice of atoms, a molten phase is formed and rapidly quenched. This results in an ion track. To determine the radius of such a track, the energy of the lattice atoms must be determined. This is done as follows [[44]]:

$$E_a=\int_0^{T_a} C_a(T')dT' \tag{55}$$

where E_a is the energy of the atom and T_a is the temperature of the lattice atom. When this energy exceeds the energy corresponding to the lattice melting temperature, $E_a(T_m)$, plus the latent heat of fusion, L_{hf}, the lattice up to that point is considered molten. Thus, by checking the energy of each lattice point the molten radius can be determined.

2.1.2. Model Results. Using the i-TS model, the track radius as a function of ion S_e can be determined. For these calculations, the S_e ranged from 2.72 – 10.35 keV nm^{-1} in SiO_2 and 3.05 – 11.09 keV nm^{-1} in CaF_2. This range was created by variation of the Ni^{6+} ion energy. Because of this, creation of a wider range of S_e would prove to be difficult. The results of the calculations can be seen in Figure 2.2. Through examination of these plots,

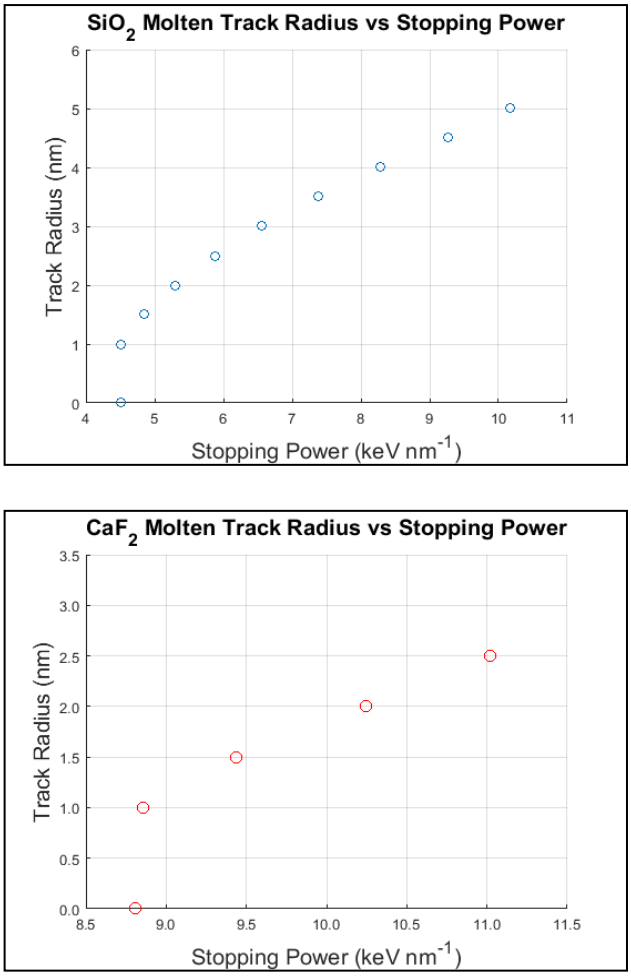

Figure 2.2 Molten track radii results. The molten track radii were calculated by the i-TS model and can be seen for (top) SiO_2 and (bottom) CaF_2.

the threshold S_e (S_{th}) for SiO_2 and CaF_2 can be determined; they are ≈4.5 keV nm^{-1} and ≈9 keV nm^{-1} respectively. The S_{th} indicates that for ion energies with $S_e<S_{th}$ no tracks are produced, hence the abrupt appearance of increasing track radii in both plots.

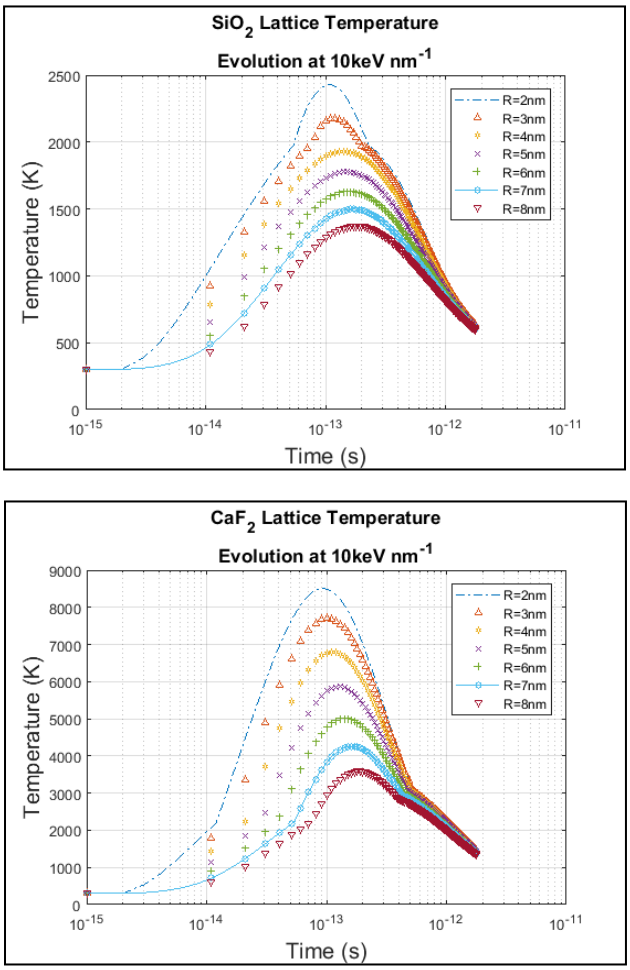

Figure 2.3. Lattice temperature evolution. The evolution of the lattice temperature with respect to time as calculated by the i-TS model for (top) SiO_2 and (bottom) CaF_2.

Additionally, the temperature evolution of the lattice with respect to time can be determined. This can be seen plotted for various radial distances in Figure 2.3. 10 keV nm^{-}

[1] was selected as the S_e for these plots. It can be observed that the maximum temperature for both materials occurs at approximately 100 fs. In SiO_2 the maximum temperature is nearly 2500 K in contrast to the approximately 8500 K in CaF_2.

2.1.3. Model Comparison and Discussion. The i-TS model has been used several times in the past to attempt to calculate the radii of ion tracks given particular incident ions [[41], [42], [44], [59]–[61], [65]]. Each attempt to apply the model varies certain parameters in hopes of improving model accuracy, applying the model to a different material, or determining a different model parameter such as λ. This makes it possible to compare this present attempt to calculate ion track radii for SiO_2 and CaF_2 to other studies. For instance, the ion track radii vs. S_e for SiO_2 can be compared to the work of Toulemonde et al. [[30]]. This can be seen in Figure 2.4. Qualitatively, the present work and that of Toulemonde et al. agrees very well. It can be seen however that the radii calculated in the present work appears to increase more rapidly as a function of S_e than the other. Additionally, the S_{th} determined by Toulemonde et al. appears to be ≈2.5 keV nm^{-1} whereas the present work indicates a S_{th} of 4.5 keV nm^{-1}.

Similarly, the plot for CaF2 can be compared to that of Dufor et al. (Figure 2.5) [[44]]. Unfortunately, this comparison is limited due to the range of Se used in the calculation. It again appears that the track radius increases at a greater rate than the work of Dufor et al. Additionally, the calculated S_{th} value appears to be approximately 4 keV nm^{-1} higher, being calculated at approximately 8.8 keV nm^{-1}.

In a similar manner, the temporal evolution of lattice temperature can be compared to previous studies (Figures 2.6 and 2.7). In both cases, the temperature appears to peak

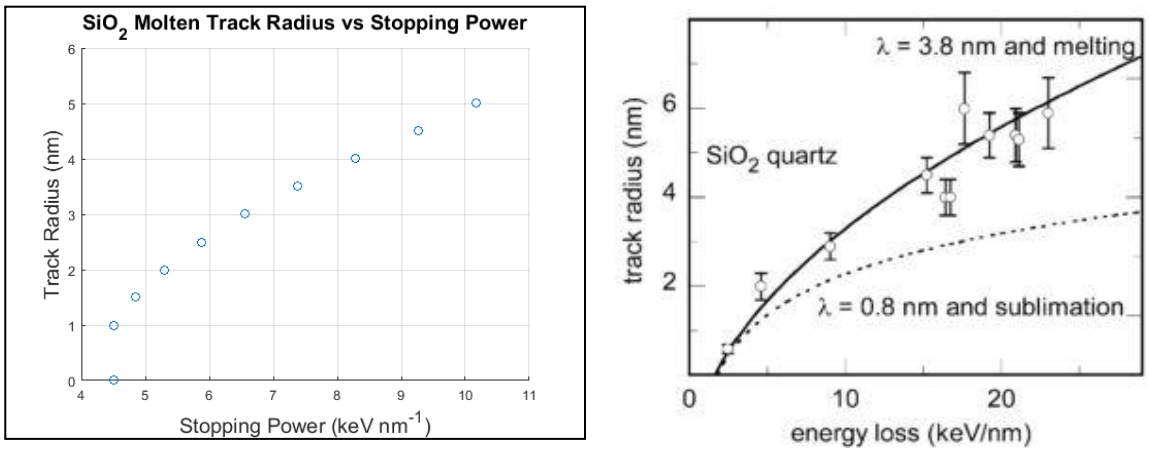

Figure 2.4. A comparison of the track radii vs. S_e plots for SiO_2. The present work (left) is compared to that of Toulemonde et al. (right) [[30]].

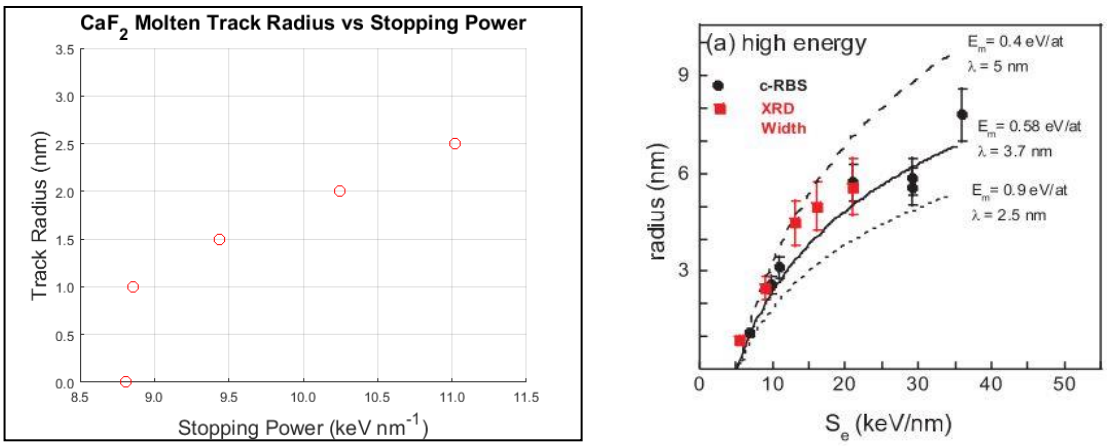

Figure 2.5. A comparison of the track radii vs. S_e plots for CaF_2. The present work (left) is compared to that of Dufor et al. [[44]].

around 10^{-13} s, or 100 fs. The main difference in both cases is that the temperature of the present work decreases more quickly than in the literature models. Additionally, the highest temperature of the CaF_2 is almost 3000 K higher than that of Dufor et al. [[44], [65]].

These particular examples create an apparent discrepancy in the calculated S_{th} and that determined from literature. This discrepancy is slightly misleading for a few reasons. The S_{th} for both SiO_2 and CaF2 has been reported several times. The determination of S_{th} has been performed through a variety of techniques each leading to a slightly different value of S_{th} [[68]]. These techniques can include x-ray diffraction and AFM amongst other things. Values for S_{th} for SiO_2 have been reported ranging from 2 keV nm^{-1} up to 5 keV nm^{-1} and at several intervals in between [[28], [30], [37], [43], [69]]. Similarly, the S_{th} values for CaF_2 have been reported in a range from 2.6 keV nm^{-1} to 6 keV nm^{-1} [[28], [44], [68], [69]]. This range of S_{th} values can be attributed to what is known as the Velocity

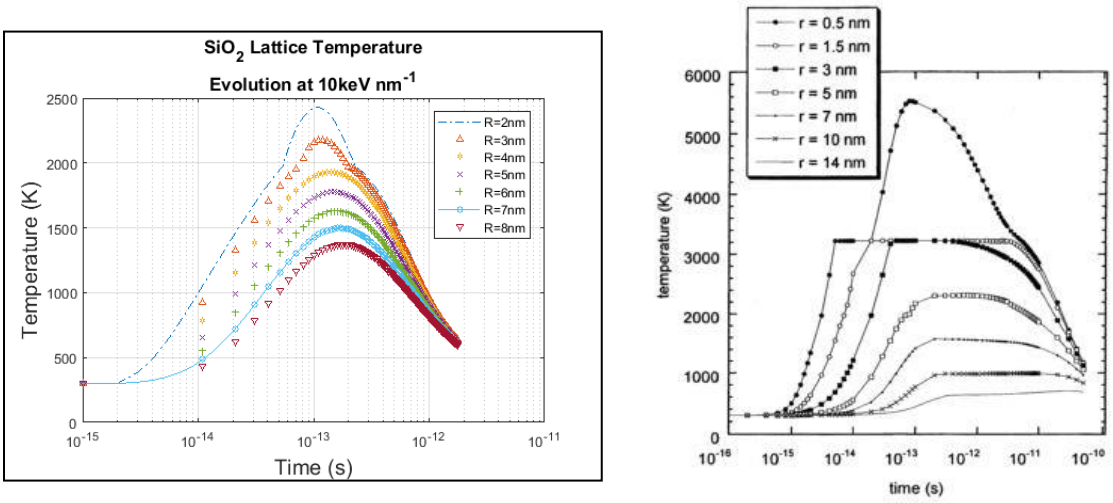

Figure 2.6. A comparison of evolution of lattice temperature in SiO_2. (Left) the present work is compared to (right) that of Toulemonde et al. [[65]]. The plot on the right demonstrates temperature evolution at a S_e of 22 keV nm^{-1}.

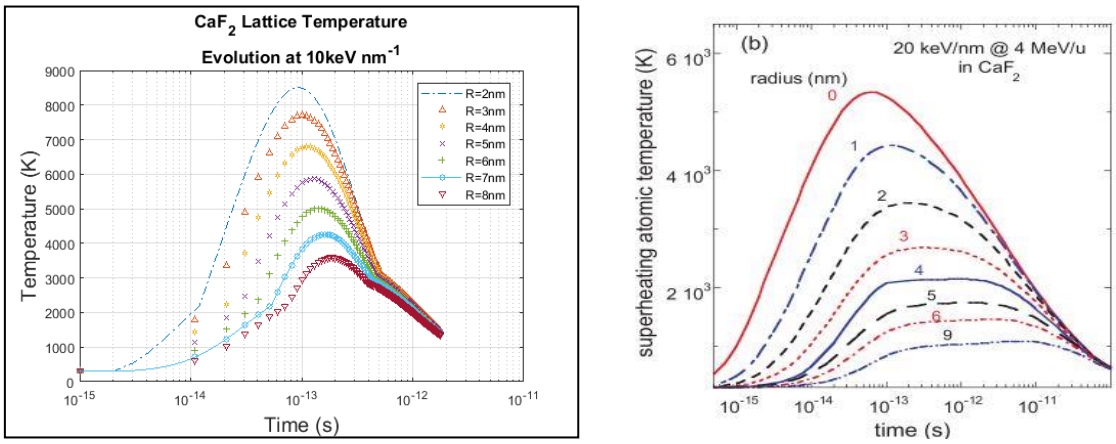

Figure 2.7. A comparison of evolution of lattice temperature in CaF_2. (Left) the present work is compared to (right) that of Dufor et al. [[44]].

Effect [[30]]. The Velocity Effect describes how with decreasing ion beam velocity, or ion energy (MeV u-1), the S_{th} is lowered. Conversely, as the ion energy increases so does S_{th}. With this in mind, the calculation of S_{th} in the present work falls within the acceptable range for SiO_2. Unfortunately, the calculated S_{th} for CaF_2 is higher than the accepted range.

The selection of the thermal properties of CaF_2 is likely the root of this issue. This is supported by the fact that the maximum temperature for a lower S_e in CaF_2 is nearly 3000 K higher than that reported in literature [[44]]. When the Lagrangian was applied for selection of K_a and C_a it sampled only 4 respective data points. The function generated likely resulted in fairly inaccurate values for both properties. The more rapid rise of the track radius in SiO_2 could be attributed to the selection of its thermal properties as well. However, the rapid rise of track radii in both materials could also be a result of the selected Bethe formula for S_e. The Bethe formula could be improved by the addition of the Barkas-Andersen effect and the Bloch correction. Since the present work is focused on the effects

of ion tracks in SiO_2, the resolution of thermal property selection for CaF_2 is left to future research. With relatively good qualitative agreement and some discrepancy due to the Velocity Effect, the corrections for the Bethe formula are also left for future work.

The i-TS model has several applications which align with current research goals. It can be used to verify track sizes measured by other measurement techniques. It can also be tailored to other materials – serving as a tool for S_{th} prediction. If a reliable method of understanding the distribution of ions in a particular fluence is created, the model may also be used to help predict track separation. The alteration of phonon transport and phononic properties may then also be predicted as a result.

2.2. SRIM/TRIM MODELING

The Stopping and Range of Ions in Matter is a group of codes used to calculate the stopping power and range of ions as they interact with matter [[58]]. The code was developed by J. Ziegler, M. Ziegler, and J. Biersack. This code performs a 'TRIM', or Transport of Ions in Matter, calculation. The main purpose of its use was to determine the stopping power and range of the Ni^{6+} ions as they interacted with the SiO_2 and CaF_2 samples. The results of this simulation are seen in Figure 2.8. Based on these simulations, the Ni^{6+} ions would result in a track with projected range of approximately 1500 nm in SiO_2. This is the distance at which the S_e of the ions drops below the threshold of 4.5 keV nm^{-1}.

Once a relationship between phonon confinement and track separation is established, a study could be performed to quantify the effects of ion track depth on phonon transport. Then, a coupled use of the i-TS and SRIM/TRIM models could result in a

simulation package which calculates the full extent of sizing and spacing on phonon transport.

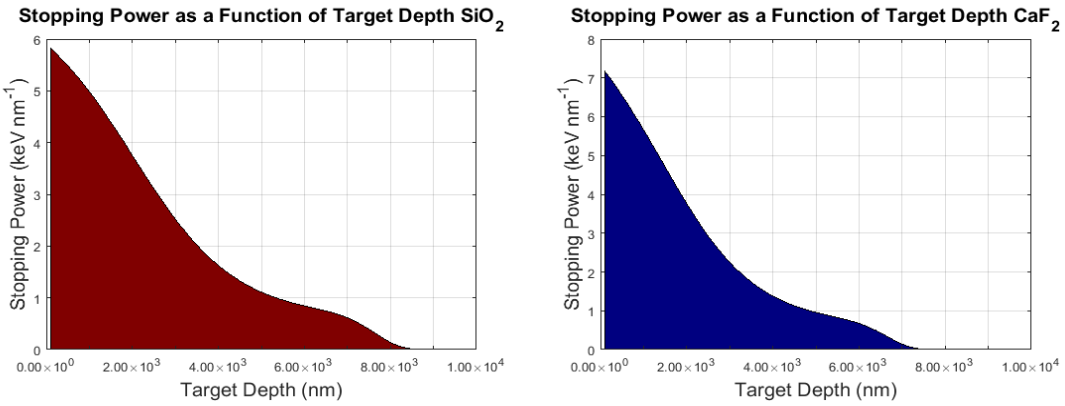

Figure 2.8. The results of a TRIM calculation using SRIM. This simulation calculates the S_e as a function of target depth.

3. ION BEAM IRRADIATION, RESULTS, AND DISCUSSION

Multiple Z- and Y-cut α-quartz single crystals were irradiated at various fluences in the Ion Beam Materials Laboratory (IBML) at the University of Tennessee Knoxville (UTK) [[36]]. These crystals were purchased from the MTI Corporation. Two different cuts of crystal were selected so that the effects of ion tracks could be understood along different crystallographic directions. Following irradiation, the crystal samples were examined using an Atomic Force Microscope and a confocal Raman microscope. The results of these measurements and related discussion are herein presented.

3.1. ION BEAM IRRADIATION

A total of 21 single crystal were irradiated in the IBML at UTK [[36]]. These crystals were irradiated at varying nominal fluence values of 1.0×10^{9}, 1.0×10^{10}, and 1.0×10^{12} ions cm^{-2}. Four Z-cut samples were irradiated at each fluence value while three Y-Cut samples were irradiated at each fluence. It is suspected that ion track size and spacing will both have impacts on phonon confinement and transport. In order to attempt to control the spacing of the tracks, multiple fluence values were used.

Since fluence gives the number of ions per unit of area (ions cm^{-2}), the expected ion separation, and therefore track separation, could be predicted. The method of prediction is as follows. An assumption is made that each ion track, i, is surrounded by neighborhood of area, A_i, which includes the cross-sectional area of the track and some surrounding crystalline material. The sum of all individual track areas is then equal to the crystal cross sectional area, A_{tot}.

$$\sum_i A_i = A_{tot} \tag{56}$$

If the cross-sectional area is then divided by the number of tracks, an average area per track, $\langle A \rangle$, can be determined.

$$\therefore \langle A \rangle = \frac{A_{tot}}{N} \tag{57}$$

With the knowledge that the fluence is the number of particles per unit area, it can be shown that the average area associated with an ion track is equivalent to the reciprocal of the fluence, Φ.

$$\langle A \rangle = \frac{A_{tot}}{N} = \frac{1}{\Phi} \tag{58}$$

A further assumption is made that the cross-sectional area associated with an ion track is circular. Thus, the effective radius of this area corresponds to the track separation. As this radius is associated with an average area, it is termed the root-mean-square radius (RMS) or average radius, $\sqrt{r^2}$. The RMS value has been tabulated for various fluence values as seen in Table 3.1.

$$\langle A \rangle = \pi \langle r^2 \rangle \tag{59}$$

$$\therefore \pi \langle r^2 \rangle = \frac{1}{\Phi} \tag{60}$$

$$\therefore \sqrt{\langle r^2 \rangle} = \frac{1}{\sqrt{\pi \Phi}} \tag{61}$$

Table 3.1 reveals why the nominal fluence values were chosen. The fluence of 1.0×10^{9} ions cm^{-2} was selected so that the tracks would be more isolated – having greater separation between them. 1.0×10^{10} ions cm^{-2} allows for a closer proximity of ion tracks

Table 3.1. Results of the RMS calculation for various fluence values.

Fluence	RMS	RMS
ions cm^{-2}	cm	nm
1.00×10^{9}	1.8×10^{-5}	178.4
5.00×10^{9}	8.0×10^{-6}	79.8
1.00×10^{10}	5.6×10^{-6}	56.4
5.00×10^{10}	2.5×10^{-6}	25.2
1.00×10^{11}	1.8×10^{-6}	17.8
5.00×10^{11}	8.0×10^{-7}	8.0
1.00×10^{12}	5.6×10^{-7}	5.6
5.00×10^{12}	2.5×10^{-7}	2.5

while still maintaining separation. The fluence of 1.0×10^{12} ions cm^{-2} leads to tracks which are separated by only a few nanometers. This is on the same order of magnitude as the actual track radii. It is between 10^{11} and 10^{12} ions cm^{-2} that the most significant effects of phonon confinement effects are expected.

These fluence values are significantly lower than the values typically produced by an accelerator. To achieve them, the Faraday cup – a conductive cup which collects charge, hence measures beam current – at the IBML was augmented with a pico-ammeter to

measure beam currents at the low levels necessary to produce the required fluence. This pico-ammeter was used to allow the current produced by the ions to be measured. The relationship between fluence and current can be seen in Equation 62. Here t is the time of measurement, *I* is the current which is measured, e is the elementary charge, and Φ is the ion fluence.

$$\frac{\Phi}{t} = \frac{I}{e} \tag{62}$$

3.2. ATOMIC FORCE MICROSCOPY

Following irradiation, a Digital Instruments Nanoscope IIIa was used to examine the crystal surface (Figure 3.1). In atomic force microscopy, a laser is shone onto the upper surface of a micro-machined cantilever probe. This probe has a sharp tip and is mounted to a piezoelectric actuator. The laser is reflected from the tip to a position-sensitive photo detector. AFM is performed in three main modes: non-contact, contact, and tapping. In non-contact mode the probe is kept at a constant distance from the sample surface by measuring the potential difference between the sample and the probe. In contact mode the probe is allowed to contact the sample surface and the deflection in the cantilever is measured as the probe is moved. In tapping mode, the cantilever is oscillated via the laser near its natural resonance frequency. Perturbations in the frequency can result from contact with the sample surface or interatomic forces [[70]]. In all cases, the laser is reflected from the probe to the photo detector. The displacements of the laser are interpreted as different surface features depending on the mode used. With some methods of AFM, displacements as small as 10^{-4} Å could be measured [[71]].

Using tapping mode and the Digital Instruments Nanoscope, the Full Width at Half Maximum (FWHM) and height of the hillocks created by the ions could be measured. These results are summarized in Table 3.2. Additionally, when the AFM measurements were being performed, it was observed that less hillocks, and therefore ion tracks, were

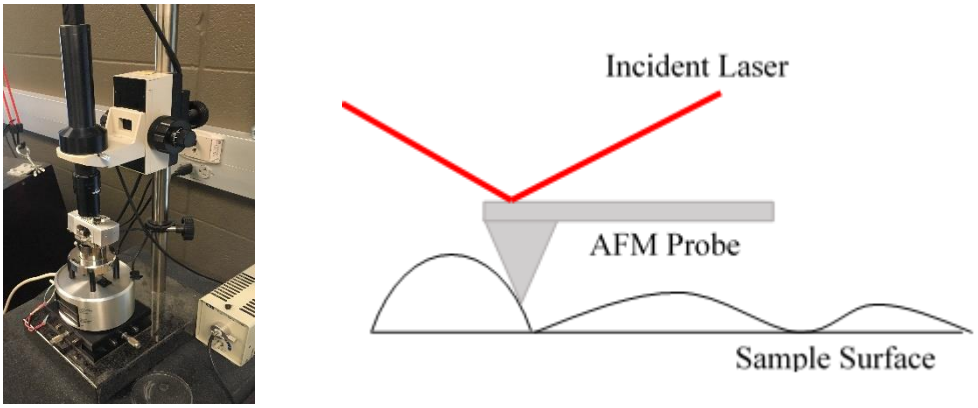

Figure 3.1. AFM depiction. (Left) The Digital Instruments Nanoscope IIIa used for AFM measurements. (Right) A simple illustration depicting the AFM principle for measuring topography; an incident laser is reflected off of a probe which interacts with the sample surface in three different manners.

present than expected. This prompted a calculation of the actual observed or measured fluence. This calculation was performed by simply counting the number of hillocks present in a given area. This information is also presented in Table 3.2. In addition, a few scans of the crystal samples can be seen in Figure 3.2. The parameters related to each scan shown are tabulated in Table 3.3.

Upon examination of Table 3.2 it is apparent that the measured fluence varies significantly from the nominal fluence. For the Z-cut, all measured fluences are on the order of 10^8 ions cm^{-2}. The measured fluence for the Y-cut samples is more sporadic. For all nominal fluence values, the measured fluence is on the order of 10^9 ions cm^{-2}. Rather than increasing as expected, the measured fluence increases for the second sample but then decreases for the third sample. In addition to the variation in fluence, it was observed that the hillocks appeared to be distributed unevenly. In some scans, the hillocks were grouped close together – some appeared to be arranged in a line. In other scans the hillocks were distributed evenly in one region, but they were completely absent in others. These results indicate error in the usage of the pico-ammeter to measure fluence between 1×10^9 and 1×10^{12} ions cm^{-2}.

Table 3.2. Results of Atomic Force Microscopy.

Crystal Cut	Fluence	Measured Fluence	Fluence σ*	Average Height	Height σ	Average FWHM	FWHM σ
	ions cm^{-2}	ions cm^{-2}	ions cm^{-2}	nm	nm	nm	nm
Z-Cut	1.00×10^9	3.80×10^8	0.9×10^8	3	1	60.0	20
	1.00×10^{10}	4.00×10^8	3.0×10^8	6	3	50	15
	1.00×10^{12}	5.00×10^8	3.0×10^8	4	3	50	14
Y-Cut	1.00×10^9	1.20×10^9	1.2×10^9	5	2	40	14
	1.00×10^{10}	6.00×10^9	0.8×10^8	5	2	40	15
	1.00×10^{12}	1.10×10^9	0.2×10^9	7	5	70	40

*σ represents the standard deviation and FWHM is the Full Width at Half Maximum of the hillocks

Table 3.3. Scan parameters used to obtain AFM images.

Image*	Crystal Cut	Fluence	Scan Size	Scan Rate	Data Scale
		ions cm^{-2}	um	Hz	nm
A		1.00×10^{9}	5.284	1.969	3.000
C	Z-Cut	1.00×10^{10}	4.563	0.500	5.000
E		1.00×10^{12}	3.585	1.969	5.000
B		1.00×10^{9}	1.744	1.001	5.000
D	Y-Cut	1.00×10^{10}	5.000	1.001	5.000
F		1.00×10^{12}	2.743	1.969	5.000

*The images referred to can be seen in Figure 3.2.

3.3. RAMAN SPECTROSCOPY AND PHONON EFFECTS

Raman spectroscopy was performed on a sample of both Z- and Y-cuts for each nominal fluence value. A Horiba Xplora Plus Raman Microscope with a 785 nm laser was used with the parameters seen in Table 3.4. These measurements were taken at room temperature under ambient conditions. Both 10x and 100x magnification were used. The Raman microscope can be seen in Figure 3.3.

3.3.1. Raman Spectra. As mentioned, the Raman spectra of both Z- and Y- cuts were obtained using the Horiba microscope. The raw spectra can be seen plotted in Figure 3.4. To more adequately compare the results of the measurements, the plots were normalized to the maximum peak intensity of the lowest nominal fluence. Then, the spectra with increasing nominal fluence were shifted vertically for clarity. This can be seen in Figure 3.5.

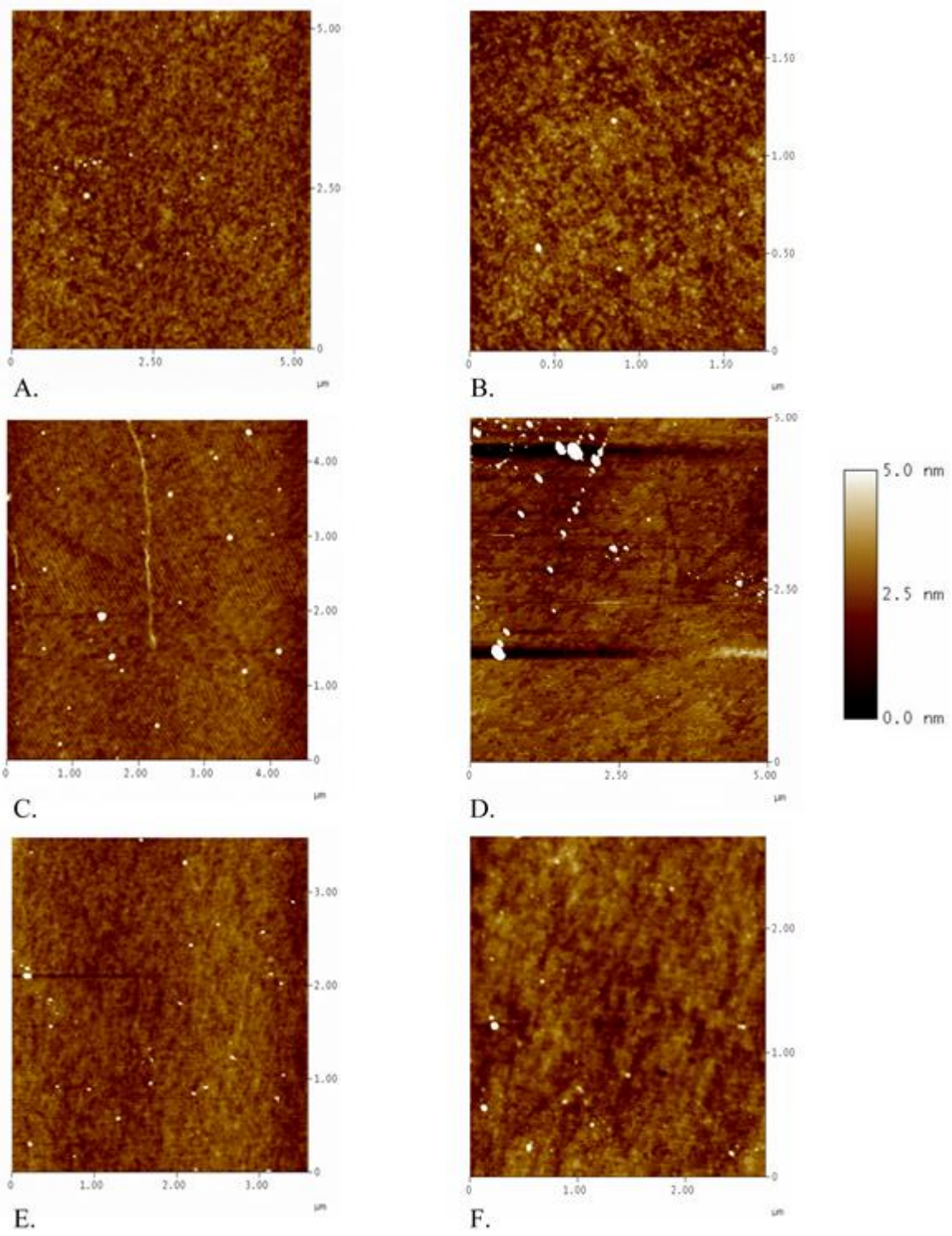

Figure 3.2. Images obtained from AFM measurements. A, C, and E are Z-cut samples. B, D, and F are Y-cut samples. Each image uses the scale shown except image A. In image A, the maximum height is 3.0 nm instead of 5.0 nm.

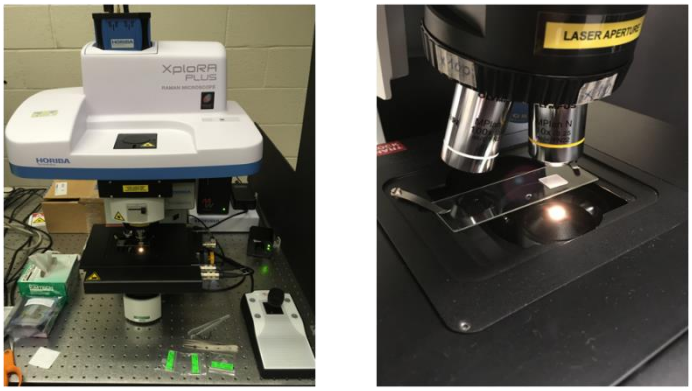

Figure 3.3. The Horiba Xplora Plus Raman Microscope. This microscope was used to obtain Raman spectra.

Table 3.4. Acquisition parameters used during Raman spectroscopy.

Acquisition Time	Accumulations	Grating	Laser Wavelength
s	-	g mm^{-1}	nm
20	20	1800	785

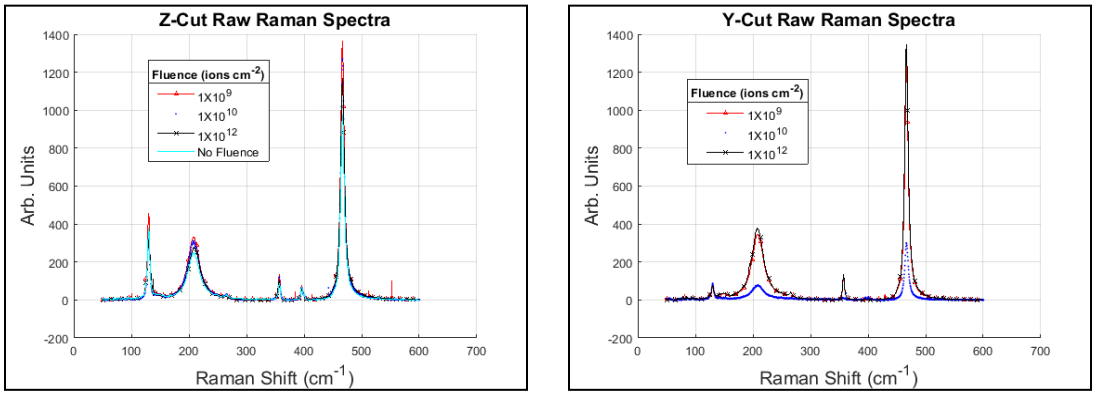

Figure 3.4. Raw Raman spectra obtained using 100x magnification.

Qualitatively, the spectra of the Z-cut crystals do not appear to change drastically. It appears that a slight shift of the peaks centered around 130 cm^{-1} and 208 cm^{-1} may have occurred. It is worth noting that for all fluence values the Z- and Y-cut crystals have slightly different spectra. More apparent changes appear in the spectra of the Y-cut crystals. As fluence increases, the peak centered near 208 cm^{-1} broadens and decreases in intensity. In fact, all peaks for the 1.0×10^{10} ions cm^{-2} fluence appear to decrease in intensity and broaden.

To understand how the peaks are quantitatively changing, peak fitting software, Fityk 0.9.8, was used to analyze various peak parameters. The first peak parameter which was analyzed was the peak center. As previously mentioned, peak shifts without broadening indicate strain in the crystal. Each peak was fit using a split Voigt function. Doing so allowed for the determination of a left and right Half Width at Half Maximum (HWHM 1 and 2 respectively). By adding these two parameters together, the FWHM of each peak could be measured. Examination of these parameters allows for the determination of peak broadening. Additionally, by dividing the HWHM 2 by the HWHM 1, a parameter describing peak asymmetry qualitatively similar to skewness could be determined. It is necessary to see if the peak is broadening asymmetrically – which could also indicate phonon confinement. An asymmetry value, J, close to 1.00 indicates that the peak is mostly symmetrical. Values greater than 1.00 indicate a positive skew, or potential broadening toward higher Raman shifts. A potential broadening towards lower shifts is indicated by J less than 1.00. These parameters are tabulated for the Z-cut samples in Table 3.5.

Upon examination of the results, it can be confirmed that peaks 1, 4, and 5 all broaden as the fluence increases from 1.0×10^{9} to 1.0×10^{12} ions cm^{-2}. Interestingly, peaks 2 and 3 actually appear to narrow. No truly significant shifting in the peaks is observed; peaks 1 and 2 blue shift by about 1 cm^{-1}, while peak 3 red shifts by approximately 1 cm^{-1}. This indicates that ion track induced stress is not likely occurring at these fluence values. The most significant changes to J occur in peaks 3 and 4. Interestingly, as peak 3 appears to narrow it also appears to become more negatively skewed. As peak 4 broadens it appears to become more symmetrical.

The analysis of the Raman spectra for the Y-cut samples yielded more interesting results. The data from the analysis is tabulated in Table 3.6. Examination with the nominal fluence values leads to sporadic results. For instance, peak 1 appears to broaden overall, but it decreases at 1.0×10^{10} ions cm^{-2} before broadening significantly at 1.0×10^{12}. A similar but opposite thing occurs with peak 3. Peak 4, in all nominal fluence values, had a very low intensity. The values for the peak were on the same scale as the noise during the counting process, making it unobservable for the 1.0×10^{12} ions cm^{-2} fluence.

While performing the Raman measurements something interesting occurred. All samples measured using Raman spectroscopy were first measured with 10x magnification and then 100x magnification. While using the 10x amplification, it appeared that peak 1, centered near 130 cm^{-1}, disappeared for the 1.0×10^{12} ions cm^{-2} fluence. When the 100x objective was used this peak was found to be present at all fluence values. This is illustrated in Figure 3.6.

The sporadic results of Table 3.6 and interesting lack of peak in the 10x magnification can both potentially be explained by the discrepancy between nominal

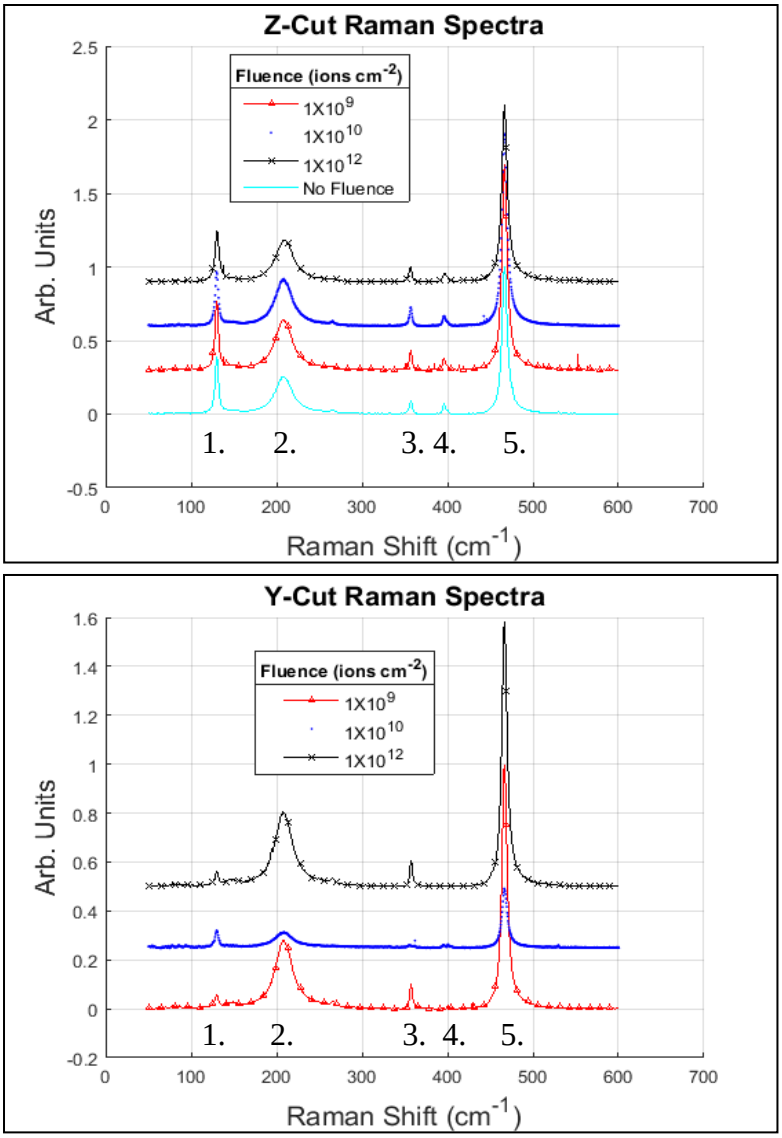

Figure 3.5. Raman spectra for both Z- and Y-cut crystal samples. The spectra have been normalized and shifted vertically for clarity. Each peak analyzed is labeled for reference.

fluence and measured fluence. From the AFM measurements it was apparent that the nominal fluence does not match what the crystals were actually exposed to. If Table 3.6 is rearranged in order of increasing measured fluence instead of nominal fluence the results seem to be more consistent with what is expected. This is tabulated in Table 3.7.

Table 3.5. Z-Cut peak parameters.

Peak	Fluence	Peak Center	Peak Center	HWHM 1	HWHM 2	FWHM	J
		cm^{-1}	THz	cm^{-1}	cm^{-1}	cm^{-1}	
1	None	129.94	3.90	2.36	2.63	5.00	1.12
1	1.00×10^{9}	129.82	3.89	2.28	2.67	4.94	1.17
1	1.00×10^{10}	129.83	3.89	2.20	2.56	4.76	1.16
1	1.00×10^{12}	130.20	3.90	2.73	3.28	6.01	1.20
2	None	208.07	6.24	11.67	12.61	24.27	1.08
2	1.00×10^{9}	208.25	6.24	11.08	12.06	23.14	1.09
2	1.00×10^{10}	208.22	6.24	10.44	11.74	22.17	1.12
2	1.00×10^{12}	209.40	6.28	11.47	11.49	22.96	1.00
3	None	357.42	10.72	2.21	1.48	3.69	0.67
3	1.00×10^{9}	357.35	10.71	2.14	1.29	3.43	0.60
3	1.00×10^{10}	356.99	10.70	1.87	0.79	2.66	0.42
3	1.00×10^{12}	356.66	10.69	2.20	0.98	3.18	0.45
4	None	395.50	11.86	1.52	0.16	1.68	0.11
4	1.00×10^{9}	395.48	11.86	1.58	0.93	2.51	0.59
4	1.00×10^{10}	395.42	11.85	1.54	0.27	1.81	0.17
4	1.00×10^{12}	396.18	11.88	1.92	1.79	3.71	0.93
5	None	466.55	13.99	3.29	4.12	7.41	1.25
5	1.00×10^{9}	466.49	13.99	3.35	4.06	7.40	1.21
5	1.00×10^{10}	466.45	13.98	3.26	4.08	7.33	1.25
5	1.00×10^{12}	466.47	13.98	3.62	4.43	8.05	1.23

Table 3.6. Y-Cut peak parameters.

Peak	Fluence	Peak Center	Peak Center	HWHM 1	HWHM 2	FWHM	J
		cm^{-1}	THz	cm^{-1}	cm^{-1}	cm^{-1}	
1	1.00×10^{9}	129.97	3.90	3.26	3.45	6.71	1.06
1	1.00×10^{10}	130.18	3.90	2.76	2.38	5.14	0.86
1	1.00×10^{12}	129.89	3.89	3.47	3.72	7.19	1.07
2	1.00×10^{9}	208.03	6.24	11.55	12.90	24.45	1.12
2	1.00×10^{10}	207.53	6.22	12.69	14.98	27.67	1.18
2	1.00×10^{12}	207.98	6.24	11.29	12.80	24.08	1.13
3	1.00×10^{9}	357.35	10.71	0.86	2.07	2.93	2.41
3	1.00×10^{10}	355.72	10.66	3.03	3.53	6.56	1.16
3	1.00×10^{12}	357.21	10.71	0.52	2.20	2.72	4.22
4	1.00×10^{9}	400.72	12.01	0.01	0.69	0.69	111.96
4	1.00×10^{10}	400.51	12.01	1.24	2.22	3.46	1.79
4	1.00×10^{12}	-	-	-	-	-	-
5	1.00×10^{09}	466.36	13.98	3.05	4.19	7.24	1.37
5	1.00×10^{10}	466.45	13.98	2.66	4.26	6.92	1.60
5	1.00×10^{12}	466.24	13.98	3.12	4.26	7.38	1.37

Now it can be seen that peaks 2, 3, and 4 all broaden systematically. It actually seems that peak 4 is now appearing with increasing fluence. In contrast, the narrowing of peaks 1 and 5 is the opposite effect to that observed in the Z-cut samples. Both the appearance and disappearance of Raman peaks with increasing fluence is not completely unexpected [[22], [34], [49], [53], [54], [57]]. For the Y-cut samples, no significant peak shifting is observed. Peak 1, 3, and 5 have the most significant changes to their J values. Peak 1 appears to become more negatively skewed while peak 5 becomes more positively

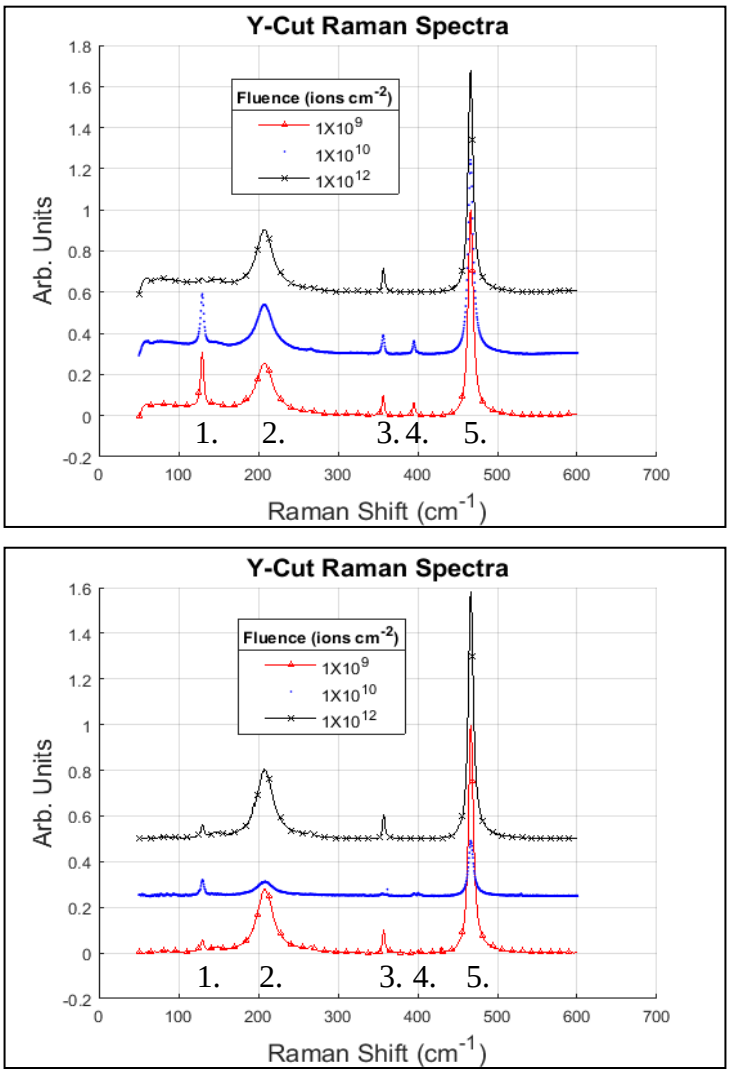

Figure 3.6. Y-Cut Raman spectra for different magnifications. The 10x magnification (top) and the 100x magnification (bottom) can both be seen.

skewed. Peak 3 goes from a large positive J towards a more symmetrical peak. Peak 4 does experience significant change in its J value, but the accuracy of it is questionable. This is again due to the intensity of peak 4 during measurements being on the same order as the noise. The rearranged Raman spectra can be seen in Figure 3.7.

Table 3.7. Rearranged Y-Cut peak parameters.

Peak	Nominal Fluence	Measured Fluence	Peak Center	Peak Center	FWHM	J
	ions cm^{-2}	ions cm^{-2}	cm^{-1}	THz	cm^{-1}	
1	1.00×10^{12}	1.10×10^{9}	129.89	3.89	7.19	1.07
1	1.00×10^{9}	1.20×10^{9}	129.97	3.90	6.71	1.06
1	1.00×10^{10}	6.00×10^{9}	130.18	3.90	5.14	0.86
2	1.00×10^{12}	1.10×10^{9}	207.98	6.24	24.08	1.13
2	1.00×10^{9}	1.20×10^{9}	208.03	6.24	24.45	1.12
2	1.00×10^{10}	6.00×10^{9}	207.53	6.22	27.67	1.18
3	1.00×10^{12}	1.10×10^{9}	357.21	10.71	2.72	4.22
3	1.00×10^{9}	1.20×10^{9}	357.35	10.71	2.93	2.41
3	1.00×10^{10}	6.00×10^{9}	355.72	10.66	6.56	1.16
4	1.00×10^{12}	1.10×10^{9}	-	-	-	-
4	1.00×10^{9}	1.20×10^{9}	400.72	12.01	0.69	111.96
4	1.00×10^{10}	6.00×10^{9}	400.51	12.01	3.46	1.79
5	1.00×10^{12}	1.10×10^{9}	466.24	13.98	7.38	1.37
5	1.00×10^{9}	1.20×10^{9}	466.36	13.98	7.24	1.37
5	1.00×10^{10}	6.00×10^{9}	466.45	13.98	6.92	1.60

The apparent lack of peak 1 in the 10x magnification also makes more sense in light of the rearranged fluence. It was noted earlier that the AFM measurements revealed uneven distribution of hillocks caused by ions. When one considers that the 1.0×10^{12} ions cm^{-2} nominal fluence actually corresponds to the lowest calculated fluence, the following proposed explanation gains some traction. The uneven random distribution of ion tracks could mean that when a Raman measurement is taken, a field of view with more or less ion tracks than the average could be present. It should be mentioned that the 100x laser spot

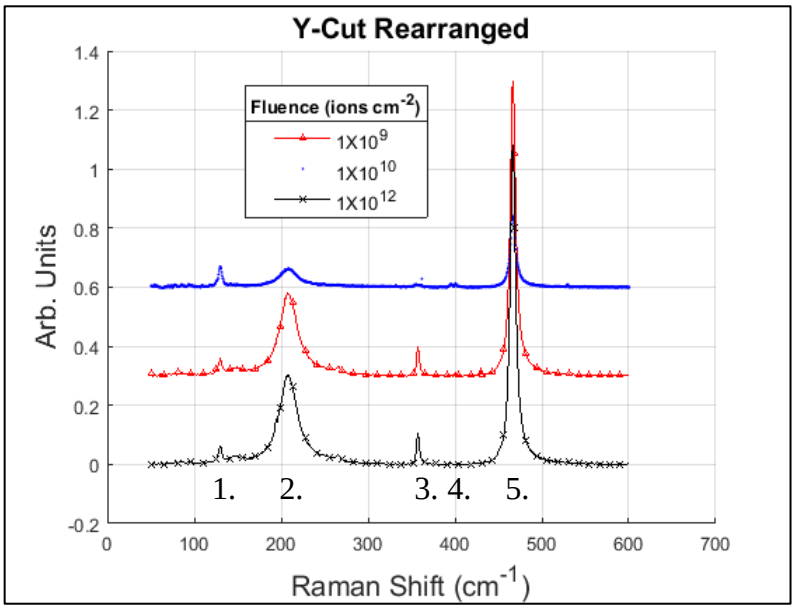

Figure 3.7. Rearranged Raman spectra of Y-Cut quartz. The Raman spectra of Y-Cut quartz was rearranged so that the highest measured fluence is the top peak – or nominally 1.0×10^{10} ions cm^{-2}.

size is also roughly 1-2 microns, comparable to the track-free areas in the more sparsely irradiated regions. The 10x objective, having a larger laser spot size, numerical aperture and field of view may have an averaging effect on the spectra. The Raman microscope may then be sampling a region without ion tracks in the 10x magnification. In the 100x magnification it may then be sampling a region with more ion tracks – leading to the presence of the first peak. A Raman mapping of the surface should be performed to confirm this theory.

In general, it can be observed that several peaks do broaden as expected. There was no significant shifting seen in the spectra observed at these fluence values. Interestingly, the effects which the ion tracks had on the Raman spectra for Z-cut crystals appeared to be

roughly opposite to that of the Y-cut. This can be seen by the broadening of peaks 1 and 5 in Z-cut quartz and the narrowing of the same peaks in the Y-cut crystals. To make these hypotheses more conclusive, the actual fluence of ions experienced by the samples needs to have varied more significantly. The accuracy of the fluence values must be improved for the results of the Raman measurements to be more accurate.

3.3.2. Effects on Raman Spectra in Relation to Phonon Dispersion Curves. As was previously mentioned, it is expected that the phonon dispersion curves will indicate how phonon transport is being altered by the presence of ion tracks. This can be done by comparing the phonon dispersion curves to the evolution of the Raman spectra. The phonon dispersion curves for α-quartz can be seen in Figure 3.8. These were produced by Strauch et al. [[47]]. In Figure 3.8 each peak observed during the Raman measurement is circled and labeled with its corresponding peak number. Raman spectroscopy only samples phonons in the Brillouin zone center; this is the region designated as Γ.

The expectation is that the phonon dispersion curves will show clear curvature or non-zero slope if the corresponding Raman peak broadens. Peak 1 is centered near 130 cm^{-1} which corresponds to a frequency of approximately 3.9 THz. Figure 3.8 indicates that the dispersion relation for this peak increases to the right of the Brillouin zone center while decreasing to its left. This should indicate broadening of the Raman peak. This is indeed the case for the Z-cut crystal as fluence increases. The slightly positive curvature in the Γ-K direction reflects the slightly increasing J. Peak 2, remains relatively flat on the dispersion curves in the Γ-K direction. The lack of broadening in this case could then be attributed to this. The curve for peak 3 has a negative curvature for both directions. This is

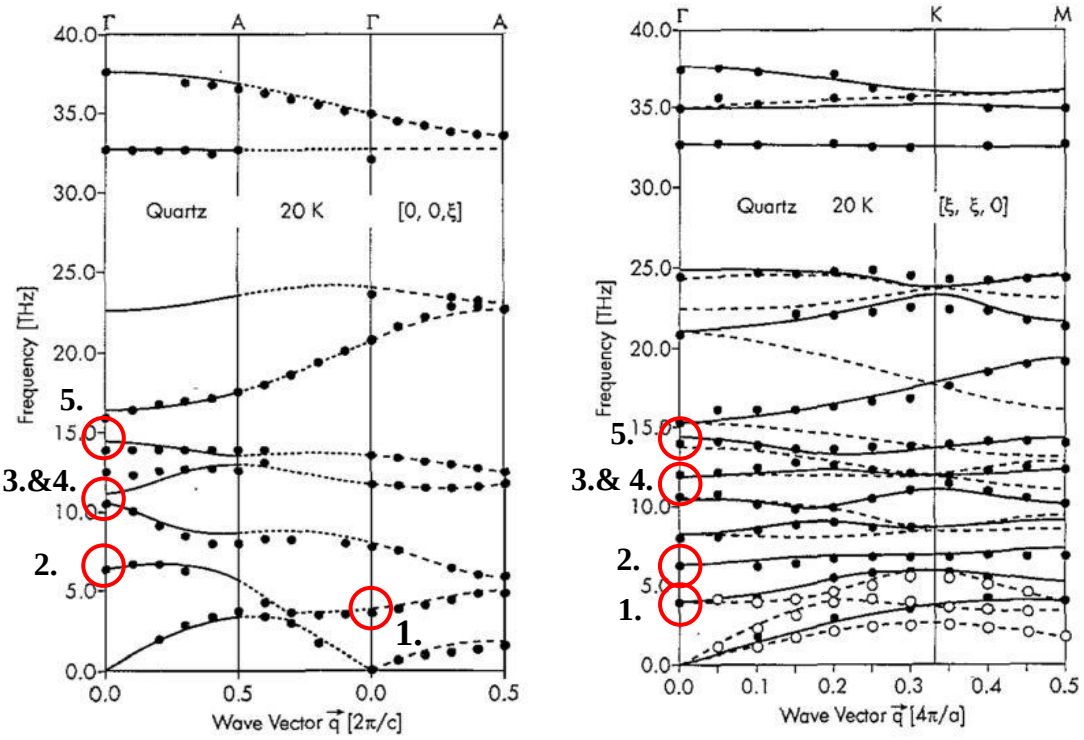

Figure 3.8. Phonon dispersion curves. These curves were calculated by Strach et al. [[47]]. The plots show the dispersion relations of α-quartz in the Γ-A and Γ-K-M directions.

directly reflected in the increasingly negative skew of peak 3.The broadening of peak 4 is reflected by the positive curvature of the dispersion curves. In both directions the dispersion relation is increasing which is reflected in the increasing J values. Finally, peak 5 is represented by a slowly decreasing slope in the dispersion curves. This peak broadens but has a relatively constant J in the Raman analysis. The dispersion curves appear to qualitatively match this.

The Y-cut crystals appear to reflect the Γ-A direction more closely than the Γ-K direction. This is especially exhibited in peaks 3 and 4. Peak 3 in the Y-cut crystal samples broadens significantly based on the measured fluence values. In addition to this, its J

becomes increasingly negative; this is directly reflected on the dispersion curves. Peak 4 appears with further irradiation in the Y-cut crystal. In doing so, its peak broadens significantly and has a positive J value. The Raman analysis of Peak 2 revealed broadening. This is also demonstrated in the Γ-A direction with the positive slope of the curve. Peaks 1 and 5, however, are not consistent with the behavior expected based on the curves. Peak 1 narrows with a decreasing J value. Peak 5 narrows instead of broadens, and the J increases rather than decreasing as expected.

The results of the Raman spectroscopy and comparison to the phonon dispersion curves reveal several promising results. In several instances, the Raman peaks broaden with increasing fluence as expected. This is also seen in the phonon dispersion curves through corresponding curvature or non-zero slope. The discrepancy between Z- and Y- cut samples illustrate how phonons propagate differently depending on the crystalline structure. The seemingly converse effects suggest that the presence of ion tracks could lead to the confinement of phonons or potentially improve their transport depending on the crystalline orientation. It must be made clear that these results must all be viewed in light of the discrepancy between nominal and measured fluence.

4. CONCLUSIONS

4.1. INELASTIC THERMAL SPIKE MODEL

An inelastic thermal spike model was created to predict ion track radii in α-quartz and calcium fluoride crystalline samples. It does so by taking into account the energy and resulting stopping powers of incident ions. This particular model was applied to Ni^{6+} ions over a range of energies and therefore electronic stopping powers. The radius is predicted by assuming a molten track is left in the wake of swift heavy Ni ions. This molten track is then assumed to be rapidly quenched, leaving behind an amorphous columnar nano structure. Given a 20 MeV Ni ion and using the S_e predicted by the SRIM/TRIM model, tracks with approximately 2.5 nm radii are predicted in α-quartz.

While the model developed for this study is qualitatively consistent with previous iterations of the i-TS model, there are certain components which could be improved upon. The most important issue arises in the selection of thermal properties for CaF_2. Only four data points were used when applying the Lagrangian for selecting the K_a and C_a of CaF_2. This leads to potentially inaccurate values and therefore a higher than expected S_{th}. Additionally, both crystals' track radii appear to rise too rapidly as S_e increases. This is potentially due to the selection of the Bethe formula. Applying the Barkas-Andersen effect and Bloch correction could potentially alleviate this issue.

Overall, the i-TS model has several applications which align with current research goals. It can be used to verify track sizes measured by other measurement techniques such as X-ray diffraction or transmission electron microscopy. The model can also be tailored to other materials which would allow it to be used as a tool for predicting S_{th}. If a reliable

method of understanding the distribution of ions in a particular fluence is created, the model may also be used to help predict track separation. The alteration of phonon transport and phononic properties may then also be predicted as a result.

4.2. RAMAN SPECTROSCOPY TO STUDY ALTERED PHONON TRANSPORT

A Horiba Xplora Plus Raman microscope was used to obtain Raman spectra for multiple Z- and Y-cut single crystalline α-quartz samples. These samples were irradiated at the Ion Beam Materials Laboratory at the University of Tennessee Knoxville. The samples were irradiated by Ni^{6+} ions at 20 MeV with nominal fluence values of 1.0×10^{9}, 1.0×10^{10}, and 1.0×10^{12} ions cm^{-2}. The goal of these measurements and irradiations was to begin to understand how increasing ion irradiation altered phonon transport. The Raman spectra were analyzed to see how five peaks changed with increasing fluence. These changes were then compared to the phonon dispersion curves of α-quartz in both the Γ-A and Γ-K direcions. The study revealed that in several instances the Raman peaks broadened with increasing ion fluence as expected. In the Z-cut crystals, peak 1 broadened by 1.02 cm^{-1}, peak 4 by 2.03 cm^{-1} and peak 5 by 0.65 cm^{-1}. In the Y-cut crystal, peak 2 broadened by 3.59 cm^{-1}, peak 3 by 3.84 cm^{-1}, and peak 4 seemingly appeared with increasing fluence. This broadening supports the notion that phonons are confined between ion tracks. This was confirmed by analyzing the phonon dispersion curves as the broadening of the peaks was accompanied by dispersion curves with non-zero slope or curvature. Additionally, in several cases, the curvature of the dispersion curves reflected the progression of the skewness of the peaks.

Unfortunately, there are several sources of error which must be resolved for better conclusiveness of this study. The first and most important source of error was encountered while performing AFM measurements. The number of hillocks counted was significantly lower than the nominal fluence expected. For instance, in the Z-cut samples, all measured fluence values were on the order of 10^8 ions cm^{-2}. This is one order of magnitude lower than the lowest nominal fluence. In the Y-cut samples, the fluence was found to be on the order of 10^9 and 10^{10} ions cm^{-2}. These fluence values are higher than those in the Z-cut crystals. However, the highest fluence was still two orders of magnitude less than the expected 1.0×10^{12} ions cm^{-2}. This indicates that the usage of a pico-ammeter in the IBML was insufficient to guarantee the desired fluence values. It is possible that the stable current reading in the pico-ammeter was dominated by current leakage or background noise which gave the false impression that the current signal was much larger than it truly was.

Other potential errors in this analysis could have come during the Raman spectroscopy of the samples. For instance, if the room varied in temperature from measurement to measurement, the measurement conditions could change from sample to sample. The measurements could be improved in reliability if the environment used in the spectroscopy was better controlled. On top of these potential sources of error, statistical noise in the sampling could affect the results as well. This is plausible because the laser used during the Raman measurements was observed to fluctuate from time to time. Overall it appeared stable, but small fluctuations during measurements could lead to statistical noise.

All things considered, Raman spectroscopy did reveal itself to be a useful means of examining how phonon transport is altered in a material. The slight alterations associated with the small variance in measured fluence points to the sensitivity of this technique. The comparison of the changing peak parameters to the dispersion curves also indicated their usefulness.

4.3. IMPLICATIONS OF ION BEAMS ON PHONONIC PROPERTIES

Examining the results of the Raman spectroscopy and phonon dispersion comparisons leads to the conclusion that ion tracks do alter phonon transport. If ion beams can be used precisely, purposeful nano-structures and patterns can be created. Nano defects are key in controlling phonons with frequencies in the GHz-THz range [[72]]. These phonons are responsible for transport of heat and hyper-sound through a system. An ion beam and its associated ion tracks could then be used for several interesting and practical applications. These defects could lead to the development of thermal diodes and 'heat cloaking' devices. Heat cloaking devices would essentially allow for the transport of heat from one side of an object to another without significant effects on the object [[72]]. This is immediately useful when one considers applications such as fusion reactors. The heat from these reactors could circumvent first wall materials altogether and be transferred directly to the coolant.

4.4. RECOMMENDATIONS FOR FUTURE WORK

There are several recommendations for future work which may be made based on previously presented conclusions. The material properties utilized in the i-TS model should be improved to improve the model results. Additionally, the correction factors should be

applied to the Bethe equation. The model could then be made more customizable or made such that it can be used to predict ion track size in other materials more easily.

Based on the AFM analysis, an actual calculation of the RMS track separation should be performed. This would allow for the effects of track spacing on phonon confinement to be taken into consideration. Once this is accomplished, phonon correlation length, *L*, calculations can be performed. This correlation length is a measure of how localized the phonon truly is, and it can be related to the total lattice disorder [[35]]. Then, the relationship between ion fluence and correlation length can be determined. Combining the predictive power of this relationship with the i-TS model and SRIM/TRIM models will allow for quantifiable predictions of phonon confinement based on ion fluence. Similarly, the thermal diffusivity or thermal conductivity of the samples should be measured. This would allow for a relationship between ion fluence and thermal diffusivity to be established. Doing this would allow for predictions of how thermal properties change with increasing ion fluence.

To better verify the results of this study, it is recommended that the irradiations be performed again. This time, the fluence values should be verified to match closely with the nominal ones. Doing this and performing the measurements again will validate the usefulness of this study and results. In addition to this, X-ray diffraction or transmission electron microscopy should be used to verify the results of the i-TS model. Once these are accomplished, a quantifiable means to associate crystallographic direction with effects on phonon transport should be created. This can be done through analysis of the differences between the Z- and Y-cut crystals.

APPENDIX A.

INELASTIC THERMAL SPIKE MATLAB CODE

The MATLAB code used to produce the i-TS model is herein presented. It is presented in two columns to conserve space.

```
%{

By:Bryant Kanies

Inelastic Thermal Spike Model


This code predicts the track radii produced in Alpha Quartz and Calcium

Fluoride when exposed to a beam of nickel ions. The experiment will use a

20 MeV nickel ion. This code evaluates the radii produced by the nickel

ion at various stopping powers. The nickel ion energies in the code range

from 10 MeV to 1000 MeV. A stopping power vs track radius plot is produced.

%}

tic


%Initialization of constants and material properites


%Discretization steps and step sizes

to = 1e-15;     %(Seconds) Energy deposition or d-ray flight time

   %ro=2.5;%nm [Dufor High resistivity, original =2.5] Rad dist. of E old

dr = 0.5;          %(nm) Spatial Step Size

dt = 5.625e-16;    %(s)  Time Step Size - 1e-15s = 1fs

leT= 1778;         %Total number of time steps

leR= 80;           %Total number of spatial steps

timevec = (1:leT);  %Vector holding time for plotting

timevec = timevec*(1e-15);  %Time vector now in s instead of fs


%Electron Material Properties

De = 2 / (1e-7)^2;  %(nm^2/s) Electron diffusivity

Ce = 1 *(1e-7)^3;   %(J/(nm^3 K)) Electron volumetric heat capacity (C*rho)

Ke = Ce*De;        %(W/(nm K))   Electron thermal conductivity

Tms = 1972;        %(K) Melting temperature of SiO2

Tmc = 1691.15;     %(K) Melting temperature of CaF2

lamS = 4;          %(nm) Electron-phonon mean free path SiO2

lamC = 3.7;        %(nm) Electron-phonon mean free path CaF2

gs = De*Ce/(lamS^2);    %(W/(nm^3K))Electron-phonon coupling parameter SiO2

gc = De*Ce/(lamC^2);    %(W/(nm^3K))Electron-phonon coupling parameter CaF2


%Energy, stopping power, and Normalization parameter calculations

E  = (10:5:2050);      %(MeV) Energy vector of Ni energies

[SeS, SeC] = bethe(E);  %(KeV/nm) Stopping Powers for SiO2 and CaF2

leS = length(SeS);      %Gives length of stopping power vector

As  = zeros(1,leS);     %Initialization of Normalization parameter for SiO2

Ac  = As;          %Initialization of Normalization parameter for CaF2

Sintegral = As;        %Vector to store integration for SiO2

Cintegral = As;        %Vector to store integration for SiO2

%Calculation of the integral values as well as normalization parameters

for i=1:leS

   [Sintegral(i), Cintegral(i)] = Dint(E(i));  %((KeV nm^2)/kg) Int. Vals

   As(i) = SeS(i)/Sintegral(i);    %(Kg/(nm^3)) Normal. Param. SiO2

   Ac(i) = SeC(i)/Cintegral(i);    %(Kg/(nm^3)) Normal. Param. CaF2

end


%Calculating the radial dose contribution using Dsi and Dca functions

mDsi = zeros(leR,leS);

mDca = mDsi;

for j = 1:leS

   for i = 1:leR
```

```
            mDsi(i,j) = Dsi(dr*i,E(j));
            mDca(i,j) = Dca(dr*i,E(j));
        end
    end

    %Conversion of stopping powers to J/nm
    % SeS = SeS.*1.60218e-16; %(J/nm) SiO2 Stopping Power
    % SeC = SeC.*1.60218e-16; %(J/nm) CaF2 Stopping Power

    %SiO2 and CaF2 properties and varialbe initialization
    ps  = 2.65 * (1e-7)^3;  %(g/nm^3) Density of SiO2
    pc  = 3.18 * (1e-7)^3;  %(g/nm^3) Density of CaF2

    %{
    The calculation requires both the atom and electron temperature for SiO2
    and CaF2. These paramteres are dependent on ion energy (Se), material
    properties, time, and electron phonon coupling. Initialized below,
    F(space,time,energy) is the electron temperature of SiO2
    G(space,time,energy) is the lattice or atom temperature of SiO2
    H(space,time,energy) is the electron temperature of CaF2
    B(space,time,energy) is the lattice or atom temperature of CaF2
    %}
    F  = zeros(leR,leT,leS);    %(K)
    G  = zeros(leR,leT,leS);    %(K)
    F(:,:,:) = 300;             %Initial Temperature set to 300 K
    G(:,:,:) = 300;             %Initial Temperature set to 300 K
    H  = zeros(leR,leT,leS);    %(K)
    B  = zeros(leR,leT,leS);    %(K)
    H(:,:,:) = 300;             %Initial Temperature set to 300 K
    B(:,:,:) = 300;             %Initial Temperature set to 300 K

    %Thermal Conductivity and Volumetric Heat Capacity
    %Initializaiton for SiO2 and CaF2
    Kas = zeros(leR,leT,leS);  %SiO2 Thermal Conductivity
    Cas = zeros(leR,leT,leS);  %SiO2 Vol. Heat Capacity
    Kas(:,:,:) = 14./G.^0.9*1e-7;       %(W/(nm K)) [Track Formation - Meftah]
    Cas(:,:,:) = (3.3e-4.*G+.65)*ps;    %(J/(nm^3 K)[Track Formation - Meftah]
    Kac = zeros(leR,leT,leS);  %Thermal coductivity of CaF2
    Kac(:,:,:) = (0.000000027951577982186251984237403570699.*B(:,:,:).^3 ...
                -0.000022656420183967626785813663213 63.*B(:,:,:).^2 ...
    +0.005317410275368425515901724928 3819.*B(:,:,:)...
                -0.230837871572470047621697685696 8)*1e-7; %(W/(nm K)) for T<400
    Cac = zeros(leR,leT,leS); %Volumetric Heat Capacity of CaF2
    Cac(:,:,:) = (0.000000000397186147186147186147186147186 14.*B.^3 -...
    0.000001082142857142857142857142857142 9.*B.^2 +...
    0.000778722943722943722943722943722 94.*B-...
    0.013766233766233766233766233766234)*(1e-7)^3; %(J/(nm^3K))

    %Stability criteria check - Ends code if criteria is not met
    Check = Ke*dt/(Ce*dr^2);
    fprintf('Check = %.3f\n',Check)
    if Check > 1/2
        fprintf('Stability Criteria not met\n')
        return
    end

    toc

    %First Set of Loops is the calculation for SiO2
    for j = 1:leS
        for n = 1:leT-1
            for i = 2:leR-1
                if G(i,n,j)>Tms
                    Kas(i,n,j)=0.01*1e-7;   %(W/(nm K)) If the temp. exceeds
                else                        %the melting temperature
```

```
                    Kas(i,n,j)=14/G(i,n,j)^0.9*1e-7;
%(W/(nmK)) Original
                end
                if G(i,n,j)>Tms
                    Cas(i,n,j) = 0.42*ps;   %(J/(nm^3 K)) If
T>melting temp
                else
                    Cas(i,n,j) = (3.3e-4.*G(i,n,j)+.65)*ps; %Same
as original
                end
                %Calculating lattice temperature and electron
temperature in K
                F(i,n+1,j)=F(i,n,j)+dt/Ce*((1/dr^2*((F(i+1,n,j)-
F(i,n,j))...
                    *(Ke*(1/i))+Ke*(F(i+1,n,j)-2*F(i,n,j)+F(i-
1,n,j)))))...
                    -gs*(F(i,n,j)-G(i,n,j))...
                    +As(j)*mDsi(i,j)*exp(-(n*dt/to))*(1/to));
                G(i,n+1,j)=G(i,n,j)+dt/Cas(i,n,j)...
                    *((1/dr^2*((G(i+1,n,j)-G(i,n,j)))...
                    *(Kas(i+1,n,j)+Kas(i,n,j)*(1/i-1)))...
                    +Kas(i,n,j)*(G(i+1,n,j)-2*G(i,n,j)+G(i-
1,n,j)))...
                    +gs*(F(i,n,j)-G(i,n,j)));
            end
            F(1,n+1,j)=F(2,n+1,j);
            G(1,n+1,j)=G(2,n+1,j);
            F(leR,n+1,j)=F(leR-1,n+1,j);
            G(leR,n+1,j)=G(leR-1,n+1,j);
        end
    end

    toc

    %Second iteration scheme calculates the temperatures for
CaF2
    for j = 1:leS
        for n = 1:leT-1
            for i = 2:leR-1
                if B(i,n,j)< 400
            Kac(i,n,j) =
(0.000000027951577982186251984237403570699*B(i,n,j)^3 ...
-
0.000022656420183967626785813663213 63*B(i,n,j)^2 ...
+0.005317410275368425515901724928381 9*B(i,n,j)...
-0.230837871572470047621697685696 8)*1e-7;
%Again in (W/(nm K))
                elseif B(i,n,j) > Tmc
                    Kac(i,n,j)=0.033*1e-7;  %(W/(nm K))
                else
                    Kac(i,n,j) = 0.05*1e-7; %(W/(nm K))
                end
                if B(i,n,j)>Tmc
                    Cac(i,n,j) = 0.042*pc;  %(J/(nm^3 K))
                else

Cac(i,n,j)=(0.000000000397186147186147186147186147186
14*B(i,n,j)^3 -...

0.000001082142857142857142857142857142
9.*B(i,n,j).^2 +...

0.000778722943722943722943722943722
94.*B(i,n,j)-...
                    0.013766233766233766233766233766234)*(1e-
7)^3;  %(J/(nm^3 K))
                end
                H(i,n+1,j)=H(i,n,j)+dt/Ce*((1/dr^2*((H(i+1,n,j)-
H(i,n,j)))...
                    *(Ke*(1/i))+Ke*(H(i+1,n,j)-2*H(i,n,j)+H(i-
1,n,j)))))...
                    -gs*(H(i,n,j)-B(i,n,j)))...
                    +Ac(j)*mDca(i,j)*exp(-(n*dt/to))*(1/to));
                B(i,n+1,j)=B(i,n,j)+dt/Cas(i,n,j)...
                    *((1/dr^2*((B(i+1,n,j)-B(i,n,j)))...
                    *(Kas(i+1,n,j)+Kas(i,n,j)*(1/i-1)))...
                    +Kas(i,n,j)*(B(i+1,n,j)-2*B(i,n,j)+B(i-1,n,j)))...
                    +gs*(H(i,n,j)-B(i,n,j)));
            end
            H(1,n+1,j)=H(2,n+1,j);
            B(1,n+1,j)=B(2,n+1,j);
            H(leR,n+1,j)=H(leR-1,n+1,j);
            B(leR,n+1,j)=B(leR-1,n+1,j);
        end
    end
```

```
toc


% Now determining the molten radius for SiO2

Rm = zeros(1,leS);  %Variable to hold the molten radius

EmeltS = ESiInt(Tms)+140; %Energy required for
melting - J/g

Em = zeros(leR, leS);

holdmax = zeros(leR,1);

for j = 1:leS

   holdmax(:,j) = max(G(:,:,j),[],2);

   for i = 1:leR

      Em(i,j) = ESiInt(holdmax(i,j));

   end

end

for j=1:leS

      i =1;

   while Em(i,j)>EmeltS

      i = i+1;

   end

   Rm(j)=dr*(i-1);

end


%Determination of the molten radius of CaF2

Rc = zeros(1,leS);

EmeltC = ECaInt(Tmc)+220; %Energy required for
melting - J/g

Ec = zeros(leR, leS);

holdmax = zeros(leR,1);

for j = 1:leS

   holdmax(:,j) = max(B(:,:,j),[],2);

   for i = 1:leR

      Ec(i,j) = ECaInt(holdmax(i,j));

   end

end

for j=1:leS

      i =1;

   while Ec(i,j)>EmeltC

      i = i+1;

   end

   Rc(j)=dr*(i-1);

end


%return


%Because the corrections to the Bethe formula have not
been applied, the

%code currently includes the same stopping power for
two different energy

%values. This means that for a given stopping power,
there are two molten

%radii calculated. To avoid this, the maximum stopping
power is found, and

%the stopping powers before this are exluded.


maxSeS = find(SeS == max(SeS(:)));  %Finds the place
of the max Se

maxSeC = find(SeC == max(SeC(:)));  %Finds the place
of the max Se

nSeS = SeS(maxSeS:end); %New vector holding
stopping power

nSeC = SeC(maxSeC:end); %New vector holding
stopping power

nRm  = Rm(maxSeS:end);  %New vector holding track
radii

nRc  = Rc(maxSeC:end);  %New vector holding track
radii

nG   = G(:,:,maxSeS:end);   %New vector used for
plotting SiO2 Temp evol.

nB   = B(:,:,maxSeC:end);   %New vector used for
plotting CaF2 Temp evol.


nRm = fliplr(nRm);

my0Rm  = find(nRm==0);

nRm(1:(length(my0Rm)-1))=[];

nSeS = fliplr(nSeS);

nSeS(1:(length(my0Rm)-1))=[];


nRc = fliplr(nRc);

my0Rc  = find(nRc==0);

nRc(1:(length(my0Rc)-1))=[];

nSeC = fliplr(nSeC);

nSeC(1:(length(my0Rc)-1))=[];
```

```
%Plotting of Molten Track Radius vs dE/dx

figure(1)

scatter(nSeS(1:15:end),nRm(1:15:end))

grid on

xlabel('Stopping Power (keV/nm)','FontSize', 15)

ylabel('Track Radius (nm)','FontSize', 15)

title('SiO2 Molten Track Radius vs Stopping
Power','FontSize', 15)



%Plotting Molten Track Radius of CaF2

figure(2)

scatter(nSeC(1:15:end),nRc(1:15:end))

grid on

xlabel('Stopping Power (keV/nm)','FontSize', 15)

ylabel('Track Radius (nm)','FontSize', 15)

title('CaF_2 Molten Track Radius vs Stopping
Power','FontSize', 15)



%Plotting Temperature Evolution

%Important note: MarkerIndices only works for
MATLAB 2016 & newer



%Finding the Se value closest to 10 KeV/nm for SiO2

SeS10Pos = find(abs(nSeS-10)<0.04);     %Finds nSeS
~=10

howcloSi = abs(10-nSeS(SeS10Pos));      %Finds abs
value of diff. w/ 10

minvalSi = min(howcloSi);               %Finds minimum
value

whichPoSi= find(howcloSi == minvalSi);  %Finds the
position of closest val.

c10Si    = SeS10Pos(whichPoSi);         %Gives the
position of the cloeset

                                        %   value to 10 KeV/nm

figure(3)

semilogx(timevec,nG(2,:,c10Si),'-.')

hold on

semilogx(timevec,nG(3,:,c10Si),'^','MarkerSize',4,'Marke
rIndices',1:10:leT)

semilogx(timevec,nG(4,:,c10Si),'h','MarkerSize',4,'Marke
rIndices',1:10:leT)

semilogx(timevec,nG(5,:,c10Si),'x','MarkerSize',4,'Marke
rIndices',1:10:leT)

semilogx(timevec,nG(6,:,c10Si),'+','MarkerSize',4,'Marke
rIndices',1:10:leT)

semilogx(timevec,nG(7,:,c10Si),'-o','MarkerSize',4,...

   'MarkerIndices',1:10:leT)

semilogx(timevec,nG(8,:,c10Si),'v','MarkerSize',4,'Marke
rIndices',1:10:leT)

grid on

xlabel('Time (s)','FontSize', 15)

ylabel('Temperature (K)','FontSize', 15)

title({'SiO_2 Lattice Temperature';'Evolution at 10keV
nm^{-1}'},...

   'FontSize', 13)

legend('R=2nm','R=3nm','R=4nm','R=5nm','R=6nm',...

   'R=7nm','R=8nm')



%Finding the Se value closest to 10 KeV/nm for CaF2

SeC10Pos = find(abs(nSeC-10)<0.04);     %Finds nSeC
~=10

howcloCa = abs(10-nSeC(SeC10Pos));      %Finds abs
value of diff. w/ 10

minvalCa = min(howcloCa);               %Finds minimum
value

whichPoCa= find(howcloCa == minvalCa);  %Finds the
position of closest val.

c10Ca    = SeC10Pos(whichPoCa);         %Gives the
position of the cloeset

                                        %   value to 10 KeV/nm



figure(4)

semilogx(timevec,nB(2,:,c10Ca),'-.')

hold on

semilogx(timevec,nB(3,:,c10Ca),'^','MarkerSize',4,'Mark
erIndices',1:10:leT)

semilogx(timevec,nB(4,:,c10Ca),'h','MarkerSize',4,'Mark
erIndices',1:10:leT)

semilogx(timevec,nB(5,:,c10Ca),'x','MarkerSize',4,'Mark
erIndices',1:10:leT)

semilogx(timevec,nB(6,:,c10Ca),'+','MarkerSize',4,'Mark
erIndices',1:10:leT)

semilogx(timevec,nB(7,:,c10Ca),'-o','MarkerSize',4,...

   'MarkerIndices',1:10:leT)
```

```
semilogx(timevec,nB(8,:,c10Ca),'v','MarkerSize',4,'MarkerIndices',1:10:leT)

grid on

xlabel('Time (s)','FontSize', 15)

ylabel('Temperature (K)','FontSize', 15)

title({'CaF_2 Lattice Temperature';'Evolution at 10keV nm^{-1}'},...

   'FontSize', 13)

legend('R=2nm','R=3nm','R=4nm','R=5nm','R=6nm',...

   'R=7nm','R=8nm')


%Plotting with only the lead values

flipRm  = nRm;  %fliplr(nRm);

flipSeS = nSeS; %fliplr(nSeS);

[myRm,inds] = unique(flipRm);

mySeS = flipSeS(inds);

figure(5)

scatter(mySeS,myRm)

grid on

xlabel('Stopping Power (keV nm^{-1})','FontSize', 15)

ylabel('Track Radius (nm)','FontSize', 15)

title('SiO_2 Molten Track Radius vs Stopping Power','FontSize', 15)

% xlim([0 12])

ylim([0 6])


flipRc  = nRc;%fliplr(nRc);

flipSeC = nSeC;%fliplr(nSeC);

[myRc,indsc] = unique(flipRc);

mySeC = flipSeC(indsc);

figure(6)

scatter(mySeC,myRc,60,'r')

grid on

xlabel('Stopping Power (keV nm^{-1})','FontSize', 15)

ylabel('Track Radius (nm)','FontSize', 15)

title('CaF_2 Molten Track Radius vs Stopping Power','FontSize', 15)

% xlim([0 12])

ylim([0 3.5])

ytickformat('%.1f')

xtickformat('%.1f')

toc


function [mySiDose] = Dsi(r,E)

%The purpose of this function is to evaluate the radial dose deposited in a

%cylinder of SiO2 from an incident ion. It is currently set up to evaluate

%the radial dose from a Nickel Ion. The function recieves a radius in nm

%and an Energy in MeV. It then calculates the dose deposited at that radius

%in J/kg. This unit is a Gray (Gy).

%6.2415e15.


%Conversion of radius from nm to cm

r = r*1e-7;


%Electron densities found by multiplying the total

%electrons for each atom by the number density

Ns = 7.9683e23; %electrons/cm^3 for SiO2


%Nickel Ion information

Z  = 28;        %Z value of Nickel

m  = 58.6934;    %Mass of nickel in u

moc= m*931.5;    %Rest mass of Nickel in MeV

beta =sqrt(1-(moc/(moc+E))^2); %Fraction of the speed of light (Energy in)

v = beta*299792458;     %Speed of ion (m/s)

vo= 2.188e8;           %Bohr's Velocity (cm/s)

vo= vo/100;            %Bhor's Velocity (m/s)

x = Z^(-2/3)*v/vo;      %Quantity used for Zeff calc

Zeff = Z*(1-exp(-x));   %Effective Z value of Nickel


%Dose Calculation

%Constants for the equation

mc2 = 0.5109989;           %Rest mass of electron (MeV)

Ys = Ns*sqrt(1.4399764)^4*1e-26*1000/(10*mc2)*1000*...

   1.6022e-19*10;         %Ne^4/mc^2 (J/cm) for SiO2

ps  = 2.65;     %g/cm^3 SiO2 - Density
```

```
ts  = r*ps;     %g/cm^2 - Range conversion for the radius
given

%Parameters based on Beta

k = 6e-6;                       %((g*KeV^(-alpha))/cm^2)

theta = k*0.01^1.079;           %Range of d ray with
E=0.01, (g/cm^2)

W = 2*mc2*beta^2/(1-beta^2)*1000;   %KeV - Max d
ray energy

if beta < 0.03

   alpha = 1.079;

else

   alpha = 1.667;

end

T   = k*W^alpha;    %Max 'range' of d ray (g/cm^2)

%D Calcuations (with correction Factor)

%The terms B and C require that r is specified in nm. To
avoid

%complication, the r in the  dose equation in the
correction terms

%will be multiplied by 1e7 which is nm/cm. This will
make the units in the

%correction factor all cancel out.

if beta < 0.03

   A = 8*beta^(1/3);

else

   A = 19*beta^(1/3);

end

B = 0.1;        %This is part of the correction factor in nm

C = 1.5+5*beta; %This is part of the correction factor in
nm


D1s = Ys*Zeff^2./(alpha*beta^2*r)*...

   ((1-(ts+theta)/(T+theta)).^(1/alpha)/(ts+theta));

Ks = A*(r*1e7-B)./C.*exp(-(r*1e7-B)./C); %Correction
factor SiO2 - unitless

mySiDose = D1s.*(1+Ks);

if isreal(mySiDose)

   mySiDose = mySiDose;

else

   mySiDose = 0;

end

end
```

```
function [myintvalSi, myintvalCa] = Dint(E)

%This function is to evaluate the integral from 0 to the
maximum radius of

%the dose function, and from 0 to time equal to infinity
for the time

%portion of the heat generation term. It recieves only one
energy value for

%a nickel ion, and returns the numerically evaluated
integral. Returns a

%value in units of (KeV nm^2 s)/kg


%Electron densities found by multiplying the total

%electrons for each atom by the number density

Ns = 7.9683e23; %electrons/cm^3 for SiO2

Nc = 9.3208e23; %electrons/cm^3 for CaF2

to = 1e-15;     %Time constant (alpha) in seconds


%Nickel Ion information

Z  = 28;        %Z value of Nickel

m  = 58.6934;   %Mass of nickel in u

moc= m*931.5;   %Rest mass of Nickel in MeV

beta =sqrt(1-(moc/(moc+E))^2); %Fraction of the speed
of light (Energy in)

v = beta*299792458;     %Speed of ion (m/s)

vo= 2.188e8;            %Bohr's Velocity (cm/s)

vo= vo/100;             %Bhor's Velocity (m/s)

x = Z^(-2/3)*v/vo;      %Quantity used for Zeff calc

Zeff = Z*(1-exp(-x));   %Effective Z value of Nickel


%Dose Calculation

%Constants for the equation

mc2 = 0.5109989;            %Rest mass of electron (MeV)

Ys = Ns*sqrt(1.4399764)^4*1e-
26*1000/(10*mc2)*1000*...

   1.6022e-19*10;       %Ne^4/mc^2 (J/cm) for SiO2

Yc = Nc*sqrt(1.4399764)^4*1e-
26*1000/(10*mc2)*1000*...

   1.6022e-19*10;       %Ne^4/mc^2 (J/cm) for CaF2

ps  = 2.65;     %g/cm^3 SiO2 - Density

pc  = 3.18;     %g/cm^3 CaF2
```

```
%Parameters based on Beta

k = 6e-6;                    %((g*KeV^(-alpha))/cm^2)

theta = k*0.01^1.079;        %Range of d ray with
E=0.01, (g/cm^2)

W = 2*mc2*beta^2/(1-beta^2)*1000;   %KeV - Max d
ray energy

if beta < 0.03

   alpha = 1.079;

else

   alpha = 1.667;

end

T   = k*W^alpha;    %Max 'range' of d ray (g/cm^2)

Rms = T/ps;         %Maximum radius of a delta ray in
SiO2 (cm)

Rmc = T/pc;         %Maximum radius of a delta ray in
CaF2 (cm)

%D Calcuations (with correction Factor)

%The terms B and C require that r is specified in nm. To
avoid

%complication, the r in the symbolic dose equation in the
correction terms

%will be multiplied by 1e-7 which is cm/nm. This will
allow the integration

%to be performed with all other r terms being specified
in cm.

if beta < 0.03

   A = 8*beta^(1/3);

else

   A = 19*beta^(1/3);

end

B = 0.1;       %nm

C = 1.5+5*beta; %nm


Gs = Ys*Zeff^2/(alpha*beta^2);

Gc = Yc*Zeff^2/(alpha*beta^2);

Ds = @(r) 2*pi*r.*Gs./r.*...

  ((1-(r.*ps+theta)./(T+theta)).^(1/alpha)./(r.*ps+theta))...

  .*(1+(A*(r*1e-7-B)/C.*exp(-(r*1e-7-B)/C)));

Dc = @(r) 2*pi*r.*Gc./r.*...

  ((1-
(r.*pc+theta)./(T+theta)).^(1/alpha)./(r.*pc+theta))...

  .*(1+(A*(r*1e-7-B)/C.*exp(-(r*1e-7-B)/C)));

%Tf = @(t) 1/to.*exp(-(t)./(to)); This integral is not
evaluated by MATLAB

%correctly. The integral can easily be solved analytically
obtaining a

%value of 1.

myDsint = integral(Ds,0.1*1e-7,Rms); %This results in a
value of J cm^2/kg

myDcint = integral(Dc,0.1*1e-7,Rmc); %This results in a
value of J cm^2/kg

myTint  =1;                  %This is in s =
integral(Tf,0,inf);

myintvalSi = myDsint*myTint*6.242e15*(1e7)^2;
%Integral val in KeVnm^2 s/kg

myintvalCa = myDcint*myTint*6.242e15*(1e7)^2;
%Integral val in KeVnm^2 s/kg

end



function [myCaDose] = Dca(r,E)

%The purpose of this function is to evaluate the radial
dose deposited in a

%cylinder of CaF2 from an incident ion. It is currently
set up to evaluate

%the radial dose from a Nickel Ion. The function
recieves a radius in nm

%and an Energy in MeV. It then calculates the dose
deposited at that radius

%in J/kg. This unit is a Gray (Gy).

%6.2415e15.


%Conversion of radius from nm to cm

r = r*1e-7;


%Electron densities found by multiplying the total

%electrons for each atom by the number density

Nc = 9.3208e23; %electrons/cm^3 for CaF2


%Nickel Ion information

Z  = 28;       %Z value of Nickel

m  = 58.6934;  %Mass of nickel in u

moc= m*931.5;  %Rest mass of Nickel in MeV

beta =sqrt(1-(moc/(moc+E))^2); %Fraction of the speed
of light (Energy in)

v = beta*299792458;    %Speed of ion (m/s)
```

```
vo= 2.188e8;          %Bohr's Velocity (cm/s)

vo= vo/100;           %Bhor's Velocity (m/s)

x = Z^(-2/3)*v/vo;    %Quantity used for Zeff calc

Zeff = Z*(1-exp(-x));  %Effective Z value of Nickel


%Dose Calculation

%Constants for the equation

mc2 = 0.5109989;          %Rest mass of electron (MeV)

Yc = Nc*sqrt(1.4399764)^4*1e-
26*1000/(10*mc2)*1000*...

   1.6022e-19*10;         %Ne^4/mc^2 (J/cm) for CaF2

pc  = 3.18;    %g/cm^3 CaF2

tc  = r*pc;    %Range conversion for the radius given
(g/cm^2)

%Parameters based on Beta

k = 6e-6;                 %((g*KeV^(-alpha))/cm^2)

theta = k*0.01^1.079;           %Range of d ray with
E=0.01, (g/cm^2)

W = 2*mc2*beta^2/(1-beta^2)*1000;  %KeV - Max d
ray energy

if beta < 0.03

   alpha = 1.079;

else

   alpha = 1.667;

end

T   = k*W^alpha;   %Max 'range' of d ray (g/cm^2)

%D Calcuations (with correction Factor)

%The terms B and C require that r is specified in nm. To
avoid

%complication, the r in the  dose equation in the
correction terms

%will be multiplied by 1e7 which is nm/cm. This will
make the units in the

%correction factor all cancel out.

if beta < 0.03

   A = 8*beta^(1/3);

else

   A = 19*beta^(1/3);

end

B = 0.1;      %This is part of the correction factor in nm

C = 1.5+5*beta; %This is part of the correction factor in
nm

D1c = Yc*Zeff^2./(alpha*beta^2*r)*...

   ((1-(tc+theta)/(T+theta)).^(1/alpha)/(tc+theta));

Kc = A*(r*1e7-B)./C.*exp(-(r*1e7-B)./C); %Correction
factor CaF2 - unitless

myCaDose = D1c.*(1+Kc);

if isreal(myCaDose)

   myCaDose = myCaDose;

else

   myCaDose = 0;

end

end


function [Spwr1, Spwr2] = bethe(E)

%This function calculates the stopping power for Nickel
given an energy

%value. It uses the Bethe formula, with a modified
expression for the Z

%value of the ion. The stopping power is returned in
units of KeV/nm for

%two materials. In this case, the materials are: 1. SiO2
and 2. CaF2


Z = 28;      %Ion Z number, in this case Nickel

m  = 58.6934; %Mass of ion in u

moc= m*931.5; %Rest mass of ion in MeV

B =sqrt(1-(moc./(moc+E)).^2); %Fraction of the speed of
light

v = B*299792458;   %Speed of ion (m/s)

vo= 2.188e8;       %Bohr's Velocity (cm/s)

vo= vo/100;        %Bhor's Velocity (m/s)

x = Z^(-2/3)*v/vo; %Effective Z based on ion energy

Zeff = Z*(1-exp(-x));


%Further Material Properties

Ns  = 7.96831e23; %Electron density of SiO2

Nc  = 9.32084e23; %Electron density of CaF2

qts = 30;         %Total Electrons in SiO2

qtc = 38;         %Total Electrons in SiO2

qo  = 16;         %Electrons due to oxygen

qsi = 14;         %Electrons due to Silicon
```

```
        qf  = 18;       %Electrons due to Fluorine
        qca = 20;       %Electrons due to Calcium
        zees = [8 14 9 20]; %Z numbers for Sio2 and CaF2
        Iene = zees;      %Initialization of mean excitaion
energies
        % Calculating Mean Excitation Energies for each
element
        if zees(:) == 1
          Iene(:) = 19;
        elseif 2 <= zees(:) <= 13
          Iene(:) = 11.2+11.7*zees(:);
        else
          Iene(:) = 52.8+8.71*zees(:);
        end
        %Calculating the mean excitation energies for each
compound
        Isi = exp(qo/qts*log(Iene(1))+qsi/qts*log(Iene(2)));
        Ica = exp(qf/qtc*log(Iene(3))+qca/qtc*log(Iene(4)));


        Spwr1 = 5.09913e-
29*Zeff.^2.*Ns./B.^2.*(log(1.022e6*B.^2./...
          (Isi*(1-B.^2)))-B.^2);                    %Stopping
power SiO2
        Spwr2 = 5.09913e-
29*Zeff.^2.*Nc./B.^2.*(log(1.022e6*B.^2./...
          (Ica*(1-B.^2)))-B.^2);                    %Stopping
power CaF2
        end


        function [eatom] = ESiInt(mytemp)
        %Receives Temperature of lattice atom and calculates
the Energy Per gram of
        % SiO2. Outputs in terms of J/g. Temperature recieved in
Kelvin
        Tms = 1972;         %(K) Melting temperature of SiO2
        ps  = 2.65 * (1e-7)^3;  %(g/nm^3) Density of SiO2


        if mytemp > Tms
          Cas = @(T)(3.3e-4*T+.65)*ps; %Same as original
          blwTm = integral(Cas,100,Tms)/ps;    %J/g
          Cas   = 0.42*ps;    %(J/(nm^3 K)) If T>melting temp
          eatom = (Cas*(mytemp-Tms))/ps + blwTm; %(J/g)
        else
          Cas = @(T)(3.3e-4*T+.65)*ps; %Same as original
          eatom = integral(Cas,100,mytemp)/ps;    %J/g
        end


        end


        function [eatom] = ECaInt(mytemp)
        %Receives Temperature of lattice atom and calculates
the Energy Per gram of
        % CaF2. Outputs in terms of J/g. Temperature recieved
in Kelvin
        Tmc = 1691.15;     %(K) Melting temperature of CaF2
        pc  = 3.18 * (1e-7)^3;  %(g/nm^3) Density of CaF2


        if mytemp > Tmc
          Cac   =
@(T)(0.00000000039718614718614718614718614718614.*T.^3 -...

0.00000108214285714285714285714285714285714285 71429.*T.^2 +...

0.00077872294372294372294372294372294.*T-...

0.013766233766233766233766233766234)*(1e-7)^3; %(J/(nm^3K))
          blwTm = integral(Cac,1,Tmc)/pc;    %J/g
          Cac   = 0.042*pc;  %(J/(nm^3 K))
          eatom = (Cac*(mytemp-Tmc))/pc + blwTm; %(J/g)
        else
          Cac   =
@(T)(0.00000000039718614718614718614718614718614.*T.^3 -...

0.0000010821428571428571428571428571429.*T.^2 +...

0.00077872294372294372294372294372294.*T-...

0.013766233766233766233766233766234)*(1e-7)^3; %(J/(nm^3K))
          eatom = integral(Cac,1,mytemp)/pc;    %J/g
        end


        end
```

APPENDIX B.

CRYSTAL PROCUREMENT INFORMATION

The α-quartz crystals purchased from the MTI Corporation. The following tables are available from:

http://www.mtixtl.com/SO-Z-101010-S1.aspx

http://www.mtixtl.com/SO-Y-101005-S1.aspx

Table B.1. Z-Cut Quartz information.

Typical Physical Properties	
Purity Wt %	Saw grade: > 99.9 Optical grade: 99.99
Crystal Structure	Hex. a= 4.914 Å c = 5.405 Å
Growth Method	Hydrothermal
Hardness	7.0 Moh's
Density	2.684 g/cm^3
Melt Point	1610 ^{o}C (phase transition point: 573.1^{o}C)
Specific Heat	0.18 cal/gm
Thermoelectric Constant	1200 mV/^{o}C @ 300 ^{o}C
Thermal Conductivity	0.0033 cal/cm/ ^{o}C
Thermal Expansion (x10^{-6}/ ^{o}C)	a_{11}: 13.71 a_{33}: 7.48
Index of Refraction	1.544
Q Value Acoustic Velocity, SAW Frequency Constant, BAW Piezoelectric Coupling	1.8 x 10^6 min. 3160 (m/sec) 1661 (kHz/mm) K^2 (%) BAW: 0.65 SAW: 0.14
Inclusion	IEC Grade II

Table B.2. Y-Cut Quartz Information.

Typical Physical Properties	
Purity Wt %	Saw grade: > 99.9 Optical grade: 99.99
Crystal Structure	Hex. a= 4.914 Å c = 5.405 Å
Growth Method	Hydrothermal
Hardness	7.0 Moh's
Density	2.684 g/cm3
Melt Point	1610 oC (phase transition point: 573.1oC)
Specific Heat	0.18 cal/gm
Thermoelectric Constant	1200 mV/oC @ 300 oC
Thermal Conductivity	0.0033 cal/cm/ oC
Thermal Expansion (x10-6/ oC)	a11: 13.71 a33: 7.48
Index of Refraction	1.544
Q Value Acoustic Velocity, SAW Frequency Constant, BAW Piezoelectric Coupling	1.8 x 106 min. 3160 (m/sec) 1661 (kHz/mm) K2 (%) BAW: 0.65 SAW: 0.14
Inclusion	IEC Grade II

BIBLIOGRAPHY

[1] L. K. Murty and I. Charit, *An Introduction to Nuclear Materials*, 2nd ed. Weinheim, Germany: Wiley-VCH Verlah GmbH & Co., 2015.

[2] L. K. Mansur, A. F. Rowcliffe, R. K. Nanstad, S. J. Zinkle, W. R. Corwin, and R. E. Stoller, "Materials needs for fusion, Generation IV fission reactors and spallation neutron sources - Similarities and differences," *J. Nucl. Mater.*, vol. 329–333, no. 1–3 PART A, pp. 166–172, 2004.

[3] D. L. Smith, "Physical sputtering model for fusion reactor first-wall materials," *J. Nucl. Mater.*, vol. 75, no. 1, pp. 20–31, 1978.

[4] A. M. Stoneham, J. R. Matthews, and I. J. Ford, "Innovative materials for fusion power plant structures: Separating functions," *J. Phys. Condens. Matter*, vol. 16, no. 27, 2004.

[5] R. C. Ewing, "Nuclear waste forms for actinides," in *Geology, Mineralogy, and Human Welfare*, 1999, vol. 96, no. March, pp. 3432–3439.

[6] K. W. D. Ledingham *et al.*, "Laser-driven photo-transmutation of 129 I — a long-lived nuclear waste product," *J. Phys. D. Appl. Phys.*, vol. 36, pp. L79–L82, 2003.

[7] O. K. Chopra, D. R. Diercks, R. R. Fabian, Z. H. Han, and Y. Y. Liu, "Managing Aging Effects on Dry Cask Storage Systems for Extended Long-Term Storage and Transportation of Used Fuel Rev. 2," Argonne, IL, 2014.

[8] H. Takano, K. Nishihara, K. Tsujimoto, T. Sasa, H. Oigawa, and T. Takizuka, "TRANSMUTATION OF LONG-LIVED RADIOACTIVE WASTE BASED ON DOUBLE-STRATA CONCEPT," *Prog. Nucl. Energy*, vol. 37, no. 1–4, pp. 371–376, 2000.

[9] J. . J. Cohen, R. L. Braun, L. L. Schwartz, and H. A. Tewef, "Economic and Environmental Evaluation of Nuclear Waste Disposal by Underground In Situ Melting," Livermore, California, 1974.

[10] F. E. Heuze, "On the Geotechnical Modeling of High-Level Nuclear Waste Disposal by Rock Melting," Livermore, California, 1981.

[11] M. Lang *et al.*, "Single-ion tracks in Gd2Zr2-xTixO7 pyrochlores irradiated with swift heavy ions," *Phys. Rev. B*, vol. 79, no. 224105, pp. 1–9, 2009.

[12] J. A. Angelo and D. Buden, "Fundamentals of Radiation Protection and Shielding," in *Space Nuclear Power*, 1st ed., Malabar, Florida: Krieger Pblushing Company, 1985, pp. 111–123.

[13] L. C. Simonsen and J. E. Nealy, "Radiation Protection for Human Missions to the Moon and Mars," Hampton, Virginia, 1991.

[14] J. A. Van Allen, "The geomagnetically trapped corpuscular radtion," *J. Geophys. Res.*, vol. 64, no. 11, pp. 1683–1689, 1959.

[15] P. Suortti and W. Thomlinson, "Medical applications of synchrotron radiation," *Phys. Med. Biol.*, vol. 48, pp. R1–R35, 2003.

[16] A. V D'Amico *et al.*, "Pretreatment Nomogram for Prostrate-Specific Antigen Recurrence After Radical Prostatectomy or External-Beam Radiation Therapy for Clinically Localized Prostate Cancer," *J. Clin. Oncol.*, vol. 17, no. 1, pp. 168–172, 1999.

[17] R. Morgan, "Fast Neutron Therapy," in *AIP Conference Proceedings*, 1972, no. 9, pp. 562–577.

[18] Z. Pastuovic, M. Jaksic, G. Kalinka, M. Novak, and A. Simon, "Deterioration of Electrical and Spectroscopic Properties of a Detector Grade Silicon Photodiode Exposed to Short Range Proton , Lithium and," *IEEE Trans. Nucl. Sci.*, vol. 56, no. 4, pp. 2457–2464, 2009.

[19] E. Akcoltekin *et al.*, "Creation of multiple nanodots by single ions," *Nat. Nanotechnol.*, vol. 2, pp. 290–294, 2007.

[20] E. H. Lee, M. B. Lewis, P. J. Blau, and L. K. Mansur, "Improved surface properties of polymer materials by multiple ion beam treatment," *J. Mater. Res.*, 1991.

[21] Y. Zhang, A. Debelle, A. Boulle, P. Kluth, and F. Tuomisto, "Advanced techniques for characterization of ion beam modified materials," *Current Opinion in Solid State and Materials Science*. 2015.

[22] N. Bajwa *et al.*, "Swift heavy ion induced modification of C60 thin films," *J. Appl. Phys.*, vol. 94, no. 1, pp. 326–333, 2003.

[23] W. Bolse, J. Conrad, F. Harbsmeier, M. Borowski, and T. Rödle, "Long and short range order in ion irradiated ceramics studied by IBA, EXAFS and Raman," *Mater. Sci. Forum*, vol. 248–249, pp. 319–325, 1997.

[24] *REFERENCE DATA SERIES No. 2 2018 Edition - Nuclear Power Reactors in the World*, 2nd ed., no. 2. Vienna, Austria: International Atomic Energy Agency, 2018.

[25] A. R. L. Fleischer, P. B. Price, and R. M. Walker, "Tracks of Charged Particles in Solids," *Science (80-.).*, vol. 149, no. 3682, pp. 383–393, 1965.

[26] Y. Seki *et al.*, "Fast neutron transmission imaging of the interior of large-scale concrete structures using a newly developed pixel-type detector," *Nucl. Instruments Methods Phys. Res. Sect. A Accel. Spectrometers, Detect. Assoc. Equip.*, vol. 870, no. February, pp. 148–155, 2017.

[27] M. C. Lagunas-Solar, "Radiation Processing of Foods: An Overview of Scientific Principles and Current Status," *J. Food Prot.*, vol. 58, no. 2, pp. 186–192, 1995.

[28] N. Itoh, D. M. Duffy, S. Khakshouri, and A. M. Stoneham, "Making tracks: electronic excitation roles in forming swift heavy ion tracks," *J. Phys. Condens. Matter*, vol. 21, no. 47, p. 474205, 2009.

[29] E. C. H. Silk and R. K. Barnes, "Examination of fission fragment tracks with an electron microscope," *Philos. Mag. A J. Theor. Exp. Appl. Phys.*, vol. 4, no. 44, pp. 970–972, 1959.

[30] M. Toulemonde, W. Assmann, C. Dufor, A. Meftah, F. Studer, and C. Trautmann, "Experimental Phenomena and Thermal Spike Model Description of Ion Tracks in Amorphisable Inorganic Insulators," Matematisk., no. January 2006, The Royal Danish Academy of Sciences and Letters, 2006, pp. 263–292.

[31] J. Callaway, "Model for lattice Thermal Conductivity at Low Temperatures," *Phys. Rev.*, vol. 113, no. 4, pp. 1046–1051, 1959.

[32] J. Campos-Delgado, L. G. Cançado, C. A. Achete, A. Jorio, and J. P. Raskin, "Raman scattering study of the phonon dispersion in twisted bilayer graphene," *Nano Res.*, vol. 6, no. 4, pp. 269–274, 2013.

[33] J. O. Orwa, K. W. Nugent, D. N. Jamieson, and S. Prawer, "Raman investigation of damage caused by deep ion implantation in diamond," *Phys. Rev. B - Condens. Matter Mater. Phys.*, vol. 62, no. 9, pp. 5461–5472, 2000.

[34] J. M. Costantini, S. Miro, F. Beuneu, and M. Toulemonde, "Swift heavy ion-beam induced amorphization and recrystallization of yttrium iron garnet," *J. Phys. Condens. Matter*, vol. 27, no. 49, 2015.

[35] J. T. Graham, Y. Zhang, and W. J. Weber, "Irradiation-induced defect formation and damage accumulation in single crystal CeO2," *J. Nucl. Mater.*, vol. 498, pp. 400–408, Jan. 2018.

[36] Y. Zhang *et al.*, "New ion beam materials laboratory for materials modification and irradiation effects research," *Nucl. Instruments Methods Phys. Res. Sect. B Beam Interact. with Mater. Atoms*, vol. 338, pp. 19–30, 2014.

[37] S. Klaumünzer, "Ion tracks in quartz and vitreous silica," *Nucl. Instruments Methods Phys. Res. Sect. B Beam Interact. with Mater. Atoms*, vol. 225, no. 1–2 SPEC. ISS., pp. 136–153, 2004.

[38] M. Boccanfuso, A. Benyagoub, K. Schwartz, and C. Trautmann, "Study of the damage produced in CaF_2 by swift heavy ion irradiation," *Nucl. Inst. Methods Phys. Res. B*, vol. 191, pp. 301–305, 2002.

[39] I. Poole, "Quartz Crystal Cuts." [Online]. Available: https://www.radio-electronics.com/info/data/crystals/quartz-crystal-cuts-at-sc-ct.php. [Accessed: 31-Jul-2018].

[40] B. Harbick, L. Suh, and J. Fong, "Closest Packed Structures," *Chemistry Libre Texts*, 2017. [Online]. Available: https://chem.libretexts.org/Textbook_Maps/Physical_and_Theoretical_Chemistry_Textbook_Maps/Supplemental_Modules_(Physical_and_Theoretical_Chemistry)/Physical_Properties_of_Matter/States_of_Matter/Properties_of_Solids/Crystal_Lattice/Closest_Pack_Structure. [Accessed: 31-Jul-2018].

[41] A. Kamarou, W. Wesch, E. Wendler, A. Undisz, and M. Rettenmayr, "Swift heavy ion irradiation of InP: Thermal spike modeling of track formation," *Phys. Rev. B - Condens. Matter Mater. Phys.*, vol. 73, no. 18, pp. 1–16, 2006.

[42] M. Toulemonde, C. Dufour, and E. Paumier, "Transient thermal process after a high-energy heavy-ion irradiation of amorphous metals and semiconductors," *Phys. Rev. B*, vol. 46, no. 22, pp. 14362–14369, 1992.

[43] O. Peña-Rodríguez, J. Manzano-Santamaría, A. Rivera, G. García, J. Olivares, and F. Agulló-López, "Kinetics of amorphization induced by swift heavy ions in α-quartz," *J. Nucl. Mater.*, vol. 430, no. 1–3, pp. 125–131, 2012.

[44] C. Dufour, V. Khomrenkov, Y. Y. Wang, Z. G. Wang, F. Aumayr, and M. Toulemonde, "An attempt to apply the inelastic thermal spike model to surface modifications of CaF2 induced by highly charged ions: Comparison to swift heavy ions effects and extension to some others material," *J. Phys. Condens. Matter*, 2017.

[45] C. Kittel, *Introduction to Solid State Physics*, Second. London: John Wiley and Sons, Inc., 1953.

[46] J. R. Ferrano, K. Nakamoto, and C. W. Brown, *Introductory Raman Spectroscopy*, Second. San Diego, CA: Elsevier Science, 2003.

[47] D. Strauch and B. Dorner, "Lattice dynamics of alpha -quartz. I. Experiment," *J. Phys. Condens. Matter*, vol. 5, no. 34, pp. 6149–6154, 1993.

[48] D. Powell, A. Compaan, J. R. Macdonald, and R. A. Forman, "Raman-scattering study of ion-implantation-produced damage in Cu2O," *Phys. Rev. B*, vol. 12, no. 1, pp. 20–25, 1975.

[49] J. D. Hunn, S. P. Withrow, C. W. White, and D. M. Hembree, "Raman scattering from MeV-ion implanted diamond," *Phys. Rev. B*, vol. 52, no. 11, pp. 8106–8111, 1995.

[50] R. Shuker and R. W. Gammon, "Raman-scattering selection-rule breaking and the density of states in amorphous materials," *Phys. Rev. Lett.*, vol. 25, no. 4, pp. 222–225, 1970.

[51] D. R. Myers, P. L. Gourley, and P. S. Peercy, "The effects of ion-implantation damage on the first-order Raman spectra of GaP," *J. Appl. Phys.*, vol. 54, no. 9, pp. 5032–5038, 1983.

[52] G. Compagnini and G. Baratta, "Polarized Raman spectroscopy in ion irradiated graphite," *Appl. Phys. Lett.*, vol. 61, no. 15, pp. 1796–1798, 1992.

[53] J. Liu *et al.*, "Raman spectroscopy of apatite irradiated with swift heavy ions with and without simultaneous exertion of high pressure," *Appl. Phys. A Mater. Sci. Process.*, vol. 91, no. 1, pp. 17–22, 2008.

[54] K. R. Nagabhushana, B. N. Lakshminarasappa, and F. Singh, "Photoluminescence and Raman studies in swift heavy ion irradiated polycrystalline aluminum oxide," *Bull. Mater. Sci.*, vol. 32, no. 5, pp. 515–519, 2009.

[55] R. J. Hemley, "Pressure Dependence of Raman Spectra of SiO2 Plymorphs: alpha-Quartz, Coesite, and Stishovite," in *High-Pressure Research in Mineral Physics*, M. Manghnani and Y. Syono, Eds. Tokyo, Japan: Terra Scientific Publishing Company, 1987, pp. 347–359.

[56] M. Kuball, "Raman spectroscopy of GaN, AlGaN and AlN for process and growth monitoring/control," *Surf. Interface Anal.*, vol. 31, no. 10, pp. 987–999, 2001.

[57] J. Liu *et al.*, "STM and Raman spectroscopic study of graphite irradiated by heavy ions," *Nucl. Instruments Methods Phys. Res. Sect. B Beam Interact. with Mater. Atoms*, vol. 212, no. 1–4, pp. 303–307, 2003.

[58] J. F. Ziegler, M. D. Ziegler, and J. P. Biersack, "The Stopping and Range of Ions in Matter." Chester, MD, 2008.

[59] A. Meftah *et al.*, "Track formation in SiO2 quartz and the thermal-spike mechanism," *Phys. Rev. B*, vol. 49, no. 18, pp. 12457–12463, 1994.

[60] C. Dufour *et al.*, "A High-Resistivity Phase Induced by Swift Heavy-Ion Irradiation of Bi - a Probe for Thermal Spike Damage," *J. Phys. C*, vol. 5, no. 26, pp. 4573–4584, 1993.

[61] M. Toulemonde, J. M. Costantini, C. Dufour, A. Meftah, E. Paumier, and F. Studer, "Track creation in SiO2 and BaFe12O19 by swift heavy ions: a thermal spike description," *Nucl. Inst. Methods Phys. Res. B*, vol. 116, no. 1–4, pp. 37–42, 1996.

[62] M. P. R. Waligorski, R. N. Hamm, and R. Katz, "Calculations of Radial Dose Distribution Around the Path of a Heavy Ion in Liquid Water," *Nucl. Tracks Radiat. Meas.*, vol. 11, no. 6, pp. 309–319, 1986.

[63] J. E. Turner, *Atoms, Radiation, and Radiation Protection*, Third., vol. 2. Oak Ridge: Wiley-VCH Verlah GmbH & Co., 2007.

[64] P. Sigmund, *Particle Penetration and Radiation Effects Volume 2*, vol. 2. 2014.

[65] M. Toulemonde, C. Dufour, A. Meftah, and E. Paumier, "Transient thermal processes in heavy ion irradiation of crystalline inorganic insulators," *Nucl. Instruments Methods Phys. Res. Sect. B Beam Interact. with Mater. Atoms*, vol. 166, pp. 903–912, 2000.

[66] J. J. Plata *et al.*, "An efficient and accurate framework for calculating lattice thermal conductivity of solids: AFLOW—AAPL Automatic Anharmonic Phonon Library," *npj Comput. Mater.*, vol. 3, no. 1, p. 45, 2017.

[67] Y.-Y. Qi, T. Zhang, Y. Cheng, X.-R. Chen, D.-Q. Wei, and L.-C. Cai, "Lattice dynamics and thermal conductivity of calcium fluoride via first-principles investigation," *J. Appl. Phys.*, vol. 119, no. 9, p. 095103, 2016.

[68] M. Karlušić *et al.*, "On the threshold for ion track formation in CaF2," *New J. Phys.*, vol. 19, no. 2, 2017.

[69] M. Toulemonde, C. Dufor, and E. Paumier, "The Ion–Matter Interaction with Swift Heavy Ions in the Light of Inelastic Thermal Spike Model," *ACTA Phys. Pol. A*, vol. 109, no. 3, pp. 311–322, 2006.

[70] N. Jalili and K. Laxminarayana, "A review of atomic force microscopy imaging systems: Application to molecular metrology and biological sciences," *Mechatronics*, vol. 14, no. 8, pp. 907–945, 2004.

[71] G. Binnig and C. F. Quate, "Atomic Force Microscope," *Phys. Rev. Lett.*, vol. 56, no. 9, pp. 930–933, 1986.

[72] M. Maldovan, "Sound and heat revolutions in phononics," *Nature*, vol. 503, no. 7475, pp. 209–217, 2013.

VITA

Bryant Alan Kanies was born in Kansas City, MO. He graduated from Harrisonville High School in May of 2013. He received his B.S. in Nuclear Engineering, a minor in Spanish, and a minor in Mathematics from Missouri University of Science and Technology in May of 2017. In December of 2018, he received his M.S. in Nuclear Engineering from Missouri University of Science and Technology.